BeFo
STIFTELSEN BERGTEKNISK FORSKNING
ROCK ENGINEERING RESEARCH FOUNDATION

INTERPRETATION OF SPECTRAL PARAMETERS FROM INDUCED POLARIZATION INVESTIGATIONS OF GEOLOGICAL MATERIALS

Sara Johansson

BeFo Report 192

STIFTELSEN BERGTEKNISK FORSKNING
ROCK ENGINEERING RESEARCH FOUNDATION

INTERPRETATION OF SPECTRAL PARAMETERS FROM INDUCED POLARIZATION INVESTIGATIONS OF GEOLOGICAL MATERIALS

Tolkning av spektrala parametrar från undersökningar av geologiska material med inducerad polarisation

Sara Johansson, Lund University

BeFo Report 192
Stockholm 2024
ISSN 1104-1773
ISRN BEFO-R-192-SE

This report is a representation of the summary chapters of the Doctoral Thesis *Geometrical controls on spectral induced polarization in time and frequency domain*, published 2019 by Sara Johansson, Lund University, ISBN: 978-91-7753-982-7.

PREFACE

What lies below the ground surface is invisible to us, but via investigations of the electrical properties in different materials, we can understand the signals that are returned from the ground when current pulses have been transmitted.

An overall conclusion in this report is that methods spanning over different length scales, from microscale via laboratory investigations to field scale investigations, are necessary to increase the understanding of how SIP-effects vary in different materials. There is currently a gap in the knowledge of how these different scales relate to each other with respect to SIP-effects. The results are a step on the way towards bridging this information gap and improve interpretation of field scale SIP-effects.

This report is based on a doctoral thesis from Lund University and the work has mainly been performed by Sara Johansson with advice and support from Torleif Dahlin, Charlotte Sparrenbom, Håkan Rosqvist and Gianluca Fiandaca along with the participants of the reference group Nils Outters, Thomas Sträng, Roger Wisén, Christel Carlsson, Lars O. Ericsson, Malin Norin, Staffan Hintze, Andreas Pfaffhuber and Per Tengborg.

The project was financed by Formas, SBUF, Lund university, Hakon Hansson Foundation and BeFo.

Stockholm

Patrik Vidstrand

FÖRORD

Det som finns under markytan är osynligt för oss, men via undersökningar av de elektriska egenskaperna i olika material kan vi förstå de signaler som returneras från marken när strömpulser har överförts.

En övergripande slutsats i denna rapport är att metoder som spänner över olika längdskalor, från mikroskala via laboratorieundersökningar till fältskalaundersökningar, är nödvändiga för att öka förståelsen för hur SIP-effekter varierar i olika material. Det finns för närvarande brister i kunskapen om hur dessa olika skalor förhåller sig till varandra med avseende på SIP-effekter. Resultaten är ett steg på vägen mot att överbrygga detta informationsgap och förbättra tolkningen av SIP-effekter i fältskalan.

Denna rapport är baserad på en doktorsavhandling från Lunds universitet och arbetet har huvudsakligen utförts av Per-Ivar Olsson, med råd och stöd från Torleif Dahlin, Charlotte Sparrenbom, Håkan Rosqvist och Gianluca Fiandaca tillsammans med deltagarna i referensgruppen Nils Outters, Thomas Sträng, Roger Wisén, Christel Carlsson, Lars O. Ericsson, Malin Norin, Staffan Hintze, Andreas Pfaffhuber och Per Tengborg.

Projektet finansierades av Formas, SBUF, Lunds universitet, Hakon Hanssons Stiftelse och BeFo.

Stockholm

Patrik Vidstrand

SUMMARY

What can we learn by transmitting electrical currents through electrodes in the ground? Geophysical methods can help us to locate the bedrock, valuable mineral ores, remains of ancient buildings and many other secrets hiding below the surface. However, it is not only the universal interest for the unknown that drives the geophysical research forward. Knowledge of, for example, fractured bedrock, contaminated groundwater or unstable ground can prepare us economically during urban expansion, not to mention to predict and prevent catastrophes such as landslides, sinkholes or contaminated drinking water. With the results of this thesis, we are moving one step closer to being able to delineate ground contaminated by the cancerogenic oil-like chemicals that were formerly used in dry cleaners all over Sweden. Furthermore, the results show that we can image the well-known geological boundary that marks the extinction of dinosaurs during the end of the Cretaceous period, as well as how ancient sea-beds and their habitats looked like millions of years ago.

What lies below the ground surface is invisible to us, but via investigations of the electrical properties in different materials, we can understand the signals that are returned from the ground when current pulses have been transmitted. The focus of this thesis is to obtain a better knowledge of how geological materials obtain electrical polarization and how the microscale material geometry influence these effects. The induced polarization effect is analogous to a capacitor in an electric circuit and arise by displacement and blockage of groundwater ions in the material pore space. The phenomenon is called Spectral Induced Polarization (SIP) and the measurements result in a spectrum showing how the induced polarization effect varies with different alternating current frequencies. The origin of the spectral dispersion is that different time scales are required for the charge-up and decay processes in different parts of the material. The charge-up time is, for instance, dependent on size distribution and shapes of the grains that builds up the geological material.

Field scale measurements of subsurface conductivity is already a well-established geophysical method, which gives two-dimensional images of how the electrical current conduction varies. The images can represent areas of several hundreds of meters length and tens to hundreds of meters depth below the ground surface. Up to three additional images can be produced by simultaneous measurements of SIP-effects, where each image corresponds to different aspects of the induced polarization effects. In this way, there is a great potential for acquiring more interpretable information about the investigated area. However, more research is needed to translate the electrical information to geological or geotechnical information.

Since SIP-effects arise at a microscopic level in geological materials, the electrical measurements have been combined with different microscopic methods in this work. Three-dimensional x-ray tomography was used to visualize how oil-like chemicals distribute around sand grains. This geometrical information was analyzed together with

laboratory measurements of SIP-effects and showed that different patterns in the distribution of the chemicals also leads to different patterns in the SIP-signals. This knowledge can be used to understand data from large-scale field surveys, which was also done as a part of the thesis work. During field-scale investigations of limestone bedrock, a core was drilled and the fossil composition in the limestone was studied in thin sections. In this way, SIP-effects in a laboratory setting could be related to, for instance, fossil composition at different bedrock levels.

An overall conclusion is that methods spanning over different length scales, from microscale via laboratory investigations to field scale investigations, are necessary to increase the understanding of how SIP-effects vary in different materials. There is currently a gap in the knowledge of how these different scales relate to each other with respect to SIP-effects. The results are a step on the way towards bridging this information gap and improve interpretation of field scale SIP-effects.

Keywords: Spectral induced polarization, Microstructure, Electrical properties, Tomography, Multiscale

SAMMANFATTNING

Vad kan vi ta reda på genom att skicka elektrisk ström genom elektroder i marken? Geofysiska metoder kan hjälpa oss att lokalisera berggrunden, värdefulla mineralfyndigheter, gamla byggnadslämningar och många andra sorters hemligheter som gömmer sig under markytan. Men det är inte bara det allmänna intresset för det okända som driver den geofysiska forskningen framåt. Kännedom om t.ex. trasigt berg, förorenat grundvatten eller instabil mark kan förbereda oss ekonomiskt vid urban utbyggnad, för att inte tala om att förutsäga och förhindra katastrofer som jordskred, slukhål eller förorenat dricksvatten. Med resultaten från denna avhandling kommer vi ett steg närmare mot att kunna lokalisera mark som förorenats av de cancerframkallande oljelika kemikalier som förr användes i kemtvättar över hela Sverige. Dessutom visar resultaten att vi kan avbilda den välkända geologiska gränsen som markerar dinosauriernas utdöende i slutet av Kritaperioden och hur havsbottnar och deras livsmiljö såg ut för miljontals år sedan.

Vad som finns under markytan är osynligt för oss, men genom att undersöka de elektriska egenskaperna i olika material kan vi förstå de signaler vi får tillbaka från marken efter att ha skickat ut strömpulser. Fokus i denna avhandling är att bättre förstå hur geologiska material laddas upp elektriskt och hur materialens geometri i mikroskala påverkar dessa effekter. Uppladdningseffekten kan liknas vid en kondensator i en elektrisk krets och uppstår genom att joner i grundvattnet förflyttas och blockeras på olika platser i materialets porsystem. Fenomenet kallas Spektral Inducerad Polarisation (SIP), och resultatet av mätningarna är ett spektrum över hur uppladdningsförmågan varierar mellan olika växelströmsfrekvenser. Den spektrala variationen beror på att uppladdningen byggs upp och klingar av under olika lång tid i olika delar av materialet. Uppladdningstiderna är bland annat beroende av storleksfördelning och former hos de korn som bygger upp det geologiska materialet.

Fältskalemätningar av markens konduktivitet är redan en väletablerad geofysisk metod som ger tvådimensionella bilder över hur den elektriska ledningsförmågan varierar. Bilderna kan motsvara områden med flera hundra meters längd och tiotals till hundratals meters djup under markytan. Genom att samtidigt mäta SIP-effekter kan ytterligare upp till tre olika bilder framställas, där var och en motsvarar olika aspekter av elektriska uppladdningseffekter. Potentialen är stor för att man på detta sätt ska kunna få ut mer tolkningsbar information om undersökningsområdet. Dock behövs mer forskning för att översätta den elektriska informationen till geologisk eller geoteknisk information.

Eftersom SIP-effekter uppstår på mikroskopisk nivå i geologiska material har de elektriska mätningarna kombinerats med olika mikroskopiska metoder i detta arbete. Tredimensionell röntgentomografi användes för att visualisera hur oljelika kemikalier fördelar sig kring sandkorn. Denna geometriska information kopplades till laboratoriemätningar av SIP-effekter och visade att olika mönster i kemikaliefördelningen också leder till olika mönster i SIP-signalerna. Denna kunskap kan

användas för att förstå mätdata från fältskaleundersökningar, vilket också gjordes som en del av avhandlingsarbetet. I samband med fältskaleundersökningar av kalkstensberggrund borrades en bergkärna upp och fossilsammansättningen i kalkstenen studerades i tunnslip. På detta sätt kunde SIP-effekter i laboratoriemiljö kopplas till bl.a. fossilsammansättningen på olika bergnivåer.

En övergripande slutsats är att arbetsmetoder på olika skalor, från mikroskala via laboratorieundersökningar till fältskaleundersökningar, är nödvändiga för att öka förståelsen för hur SIP-effekter varierar i olika material. Idag finns luckor i kunskapen om hur dessa olika skalor relaterar till varandra med avseende på SIP-effekter. Resultaten är ett steg på vägen mot att överbrygga dessa informationsluckor och leda till bättre tolkningar av SIP-effekter i fältskala.

Nyckelord: Spektral inducerad polarisation, Mikrostruktur, Elektriska egenskaper, Tomografi, Multiskala

AUTHOR PREFACE

This report is a representation of the summary chapters of the doctoral thesis *Geometrical controls on spectral induced polarization in time and frequency domain*, published 2019 by Sara Johansson, Lund University, ISBN: 978-91-7753-982-7. The doctoral thesis is compiled by the summary chapters and the following five scientific publications:

Johansson, S., Fiandaca, G. & Dahlin, T. (2015). Influence of Non-Aqueous Phase Liquid Configuration on Induced Polarization Parameters: Conceptual Models Applied to a Time-Domain Field Case Study. Journal of Applied Geophysics, 123, 295–309. https://doi.org/10.1016/j.jappgeo.2015.08.010

Johansson, S., Rossi, M., Hall, S. A., Sparrenbom, C., Hagerberg, D., Tudisco, E., Rosqvist, H. & Dahlin, T. (2019). Combining Spectral Induced Polarization with x-ray tomography to investigate the importance of DNAPL geometry in sand samples. Geophysics, 84(3), E173-E188. https://doi.org/10.1190/geo2018-0108.1

Johansson, S., Sparrenbom, C., Fiandaca, G., Lindskog, A., Olsson, P.-I., Dahlin, T. & Rosqvist, H. (2016). Investigations of a Cretaceous Limestone with Spectral Induced Polarization and Scanning Electron Microscopy. Geophysical Journal International, 208(2), 954-972. https://doi.org/10.1093/gji/ggw432

Johansson, S., Lindskog, A., Fiandaca, G. & Dahlin, T. (2019). Spectral Induced Polarization of limestone: time domain field data, frequency domain laboratory data and physicochemical rock properties. Geophysical Journal International, published online. https://doi.org/10.1093/gji/ggz504

Johansson, S., Hedblom, P., Dahlin, T. (2020). Spectral analysis of time domain induced polarization waveforms. Journal of Applied Geophysics, 177. https://doi.org/10.1016/j.jappgeo.2020.10.104037

Funding which made this work possible was provided by BeFo, Swedish Rock Engineering Research Foundation, (ref. 331) and SBUF, The Development Fund of the Swedish Construction Industry, (ref. 12719 and 13232) and Formas, The Swedish Research Council for Environment, Agricultural Sciences and Spatial Planning, provided funding for this presentation of the results (ref. 2012-1931) as part of the Geoinfra-TRUST framework (http://www.trust-geoinfra.se/). Additional funding in specific projects was provided by Sven Tyréns Stiftelse and the Royal Physiographic Society in Lund.

SYMBOLS AND UNITS

$\mathbf{E}$ [V/m]	Electric field
$\mathbf{J}$ [A/m^2]	Electric current density
$\boldsymbol{D}$ [C/m^2]	Electric charge displacement
f [Hz]	Frequency
ω [rad/s]	Angular frequency
Z^* [Ω]	Complex impedance
ρ [Ωm]	Resistivity
ρ^* [Ωm]	Complex resistivity
ρ_0 [Ωm]	Low-frequency resistivity
σ [S/m]	Conductivity
σ^* [S/m]	Complex conductivity
σ_0 [S/m]	Low-frequency conductivity
σ' [S/m]	Real part of the complex conductivity (Cartesian coordinates)
σ'' [S/m]	Imaginary part of the complex conductivity (Cartesian coordinates)
$\lvert\sigma\rvert$ [S/m]	Amplitude of the complex conductivity (Polar coordinates)
φ [rad]	Phase of the complex conductivity (Polar coordinates)
ε [F/m]	Dielectric permittivity
ε^*[F/m]	Complex dielectric permittivity
ε'[F/m]	Real part of the complex permittivity (Cartesian coordinates)
ε''[F/m]	Imaginary part of the complex permittivity (Cartesian coordinates)
ε_w^*[F/m]	Complex permittivity of pore fluid, Bruggeman-Hanai-Sen equation
ε_m^*[F/m]	Complex permittivity of mineral grains, Bruggeman-Hanai-Sen equation
θ [$unitless$]	Porosity, Bruggeman-Hanai-Sen equation
V_p [V]	Primary potential
V_s [V]	Secondary potential
m_0[V/V]	Intrinsic chargeability
c [$unitless$]	Frequency exponent of the Cole-Cole model
τ [s]	Relaxation time of the Cole-Cole model
τ_ρ [s]	Relaxation time of the Cole-Cole model, complex resistivity form
τ_σ[s]	Relaxation time of the Cole-Cole model, complex conductivity form

ABBREVIATIONS

BSE detector	Backscattered Electron detector
CPA	Constant Phase Angle
DC	Direct Current
DCIP	Direct Current resistivity and Induced Polarization
DNAPL	Dense Non-Aqueous Phase Liquid
DOI	Depth of Investigation
EDL	Electrical Double Layer
EDS	Energy Dispersive x-ray Spectroscopy
FD	Frequency Domain
IP	Induced Polarization
K-Pg boundary	Cretaceous-Paleogene boundary
LNP model	Long Narrow Pore model
MIC	Maximum Imaginary Conductivity
MPA	Maximum Phase Angle
NAPL	Non-Aqueous Phase Liquid
PCE	Tetrachloroethylene
SE detector	Secondary Electron detector
SEM	Scanning Electron Microscopy
SIP	Spectral Induced Polarization
SNP model	Small Narrow Pore model
TD	Time Domain
XRF	X-Ray Fluorescence

CONTENTS

1. INTRODUCTION

In many situations, knowledge of subsurface material properties is essential. These situations include, for instance, exploitation of previously untouched ground for construction of buildings or infrastructure development, e.g. roads, railways and tunnels. Environmental concerns are other important situations where knowledge of subsurface material properties can improve e.g. preventive measures for contaminant dispersion. Expansion of urban areas often involves re-use of land that has already been altered by human activities, for example abandoned industrial areas or landfills. In many cases, historically affected ground needs to be restored for the cause of human and environmental health. In these situations, knowledge of the local conditions beneath the ground surface is essential. Without this knowledge, constructions might not withstand forces such as flooding or landslides and authorities might not be able to predict or prevent disposal of contaminants to drinking water reserves or other sensitive environments. One method that can be used to investigate local ground conditions is the Direct Current resistivity and Induced Polarization method (DCIP). The DCIP method provides tomographic images representing the distribution of electrical properties in the ground. These properties are the resistance to current flow and the ability of the ground to become electrically charged. Recent and ongoing developments in data acquisition and processing methods (Olsson et al., 2016) have led to the possibility to recover more details than was previously possible about the electrical charge- and discharge behavior in the ground. Different aspects of this behavior, called the Spectral Induced Polarization (SIP) effect, is believed to be sensitive to a range of different material properties in the ground. Extraction of SIP parameters from tomographic DCIP surveys, measured in the Time Domain (TD), is therefore potentially an efficient way to provide more detailed information about the subsurface materials. In this way, information for better predictions could be provided in a variety of different applications.

1.1 Background

The usefulness of extracting spectral information from TD IP tomography is dependent on an understanding of what the parameters can tell us about the subsurface. With the TD IP method there are several possible pitfalls during the data acquisition and processing, which can, in the worst case, lead to erroneous results and misinterpretation of the results. High-quality data is essential for obtaining representative images of subsurface electrical properties. The demands for good data quality increases significantly from resistivity measurements to IP measurements as well as from traditional quantification of the IP response to extraction of spectral parameters (Dahlin and Leroux, 2012; Dahlin, 2014). Inverse modelling of the acquired data is needed before any interpretations can be carried out, and it is essential that the inversion model fit the data representatively. Furthermore, the acquired data must always be preprocessed prior to the inversion in order to remove erroneous data, noise and unwanted inductive coupling effects.

The final interpretation of the inversion models is often challenging even with high-quality data acquisition, data processing and inverse modelling. In many cases, reference data (e.g. drilling results) are sparse. Even if they are available, they may not be informative enough to aid the interpretation of spectral IP parameters, which are largely dependent on the microgeometrical structure in the materials. It is important with well-grounded and sound data interpretation, since insufficient knowledge can lead to rushed or implausible interpretations. Such interpretations significantly diminishes the value of the field investigation as a whole and might also harm the reputation of the method among non-experts.

While the variation of electrical resistivity in geological materials is relatively well-known, interpretation of spectral IP parameters is less intuitive. More knowledge about the variation of the SIP response in geological materials is needed. The current physical understanding of the SIP phenomenon is mainly based on research focusing on systematic laboratory measurements or mechanistic modelling of homogeneous granular materials (chapter 3). There are thus three main challenges related to the interpretation of spectral IP parameters measured with TD SIP tomography. Firstly, numerous parameters can affect the SIP response measured at a field site where most of them are usually unknown, including the microstructures of the materials. A variety of different material types can be expected at a natural field site, and there is therefore a need for a better understanding of the spectral responses of materials with microstructures other than homogeneously packed spherical grains. Secondly, field measurements are carried out at a completely different scale compared to laboratory measurements, and homogeneous properties within the inverted model cells representing a single material type can therefore often not be expected. Thirdly, a majority of the systematic laboratory research studies are carried out with frequency domain (FD) systems. Although frequency- and time domain measurements are theoretically equivalent via the Fourier transform, many practical factors can affect the assessable spectral content of TD waveforms. There are yet no systematic studies showing that equivalent spectra are actually obtained from frequency- and time domain SIP measurements.

1.2 Objectives and Aim

The main aim of this work is to investigate what information can be gained about subsurface materials, based on inverted spectral IP parameters from field scale TD IP tomography. The additional information that might be hidden in these parameters can lead to better physically founded interpretations and an increased value of the method in many applications.

The main objective is therefore to investigate the physical meaning of inverted spectral IP parameters from field scale TD IP tomography. This can be understood as an attempt to meet some of the challenges and research gaps discussed above. The main objective can therefore be broken down into two concrete objectives:

i. To investigate the effect of different microgeometrical structures on the SIP response of a material.
ii. To narrow the current gap between FD laboratory SIP research and field scale TD SIP tomography.

1.3 Limitations

The results presented in this report are limited to two kinds of applications; sandy materials contaminated with non-aqueous phase liquids (NAPLs) and lithological variation in limestones. The strategies and results of the data interpretations are however generally applicable also for other cases. The choice of the former application is mainly motivated by societal needs for better pre-investigation methods and an expressed research need within the IP community (Kemna et al., 2012). The latter application was chosen since better information about bedrock properties is needed in Swedish infrastructure projects. Limestone is a relatively common bedrock in southern Sweden at the same time as a lack of SIP experience with this type of material was identified in the scientific literature.

The data analysis in this work is limited to measured raw and processed data or inverted models. Although data inversion is an important part of the workflow, reviews or comparisons between different inversion softwares are outside the scope. However, the quality of the inversion results in terms of applicable inversion settings and data fit have been ensured throughout this work. A general understanding of how the inversion method works is needed, but a complete control over the inversion software is also outside the scope.

2. SPECTRAL INDUCED POLARIZATION

Induced polarization (IP) is a measure of the capacitive properties of materials, i.e. the ability of the ground to store electrical energy. The IP phenomenon manifests itself in Time Domain (TD) as a lingering decay of electrical potential after the transmission of a Direct Current (DC) pulse. Alternatively, the IP effect can be determined in Frequency Domain (FD) as the phase shift of an alternating current travelling through the material. Spectral induced polarization (SIP) usually refers to repeated FD measurements of the amplitude- and phase shifts with different current frequencies. However, spectral information can also be extracted from TD data by considering the shape of the voltage decay.

2.1 Time- and frequency domain IP measurements

The principle of spectral FD IP measurements is shown to the left in Figure 2.1. Alternating currents with fixed potential amplitudes are transmitted through the sample via current electrodes. Typically, a spectral range somewhere between 0.001-1000 Hz is used for the current transmission. Simultaneously, the potential difference is measured between two potential electrodes. For each frequency, the amplitude- and phase shifts between the transmitted and measured sinusoids are calculated. Together, they represent the complex resistivity of the sample, more often expressed as the (reciprocal) complex conductivity:

$$\sigma^*(\omega) = |\sigma|e^{i\omega\varphi} = \sigma'(\omega) - i\sigma''(\omega) \qquad 2.1$$

In Equation 2.1, ω (Hz) is the angular frequency, σ^* (S/m) is the complex conductivity, $|\sigma|$ (S/m) is the amplitude shift and φ (rad) is the phase shift. The complex conductivity can also be expressed in Cartesian coordinates, where σ' (S/m) is the real conductivity and σ'' (S/m) is the imaginary conductivity.

The amplitude- and phase spectra shown to the right in Figure 2.1 are examples of ideal spectral shapes obtained with spectral FD IP measurements. Features that are typically of interest in the analysis of SIP data are the size and width of the phase peak and its position on the frequency axis.

In TD measurements, DC pulses are transmitted through the material via current electrodes. The potential field arising from the current transmission is sampled continuously with another electrode pair. In Figure 2.2, the principle of TD measurements is illustrated. The TD waveform typically consists of a current square wave with a constant amplitude and regularly reversed polarity. The 50% duty cycle waveform consist of equal periods with and without current transmission, so called on- and off-time periods. It takes a certain time for the potential to reach steady-state conditions during the current on-time. Similarly, the discharge of the potential during current off-time also requires a

finite time period. The charge- and discharge processes are believed to be linear, i.e. inverses of each other. Therefore, TD IP measurements can also be performed with a 100% duty cycle, as illustrated in Figure 2.2. With this waveform, the charge- and discharge processes overlap which leads to increased signal-to-noise ratio and reduced acquisition time (Olsson *et al.*, 2015).

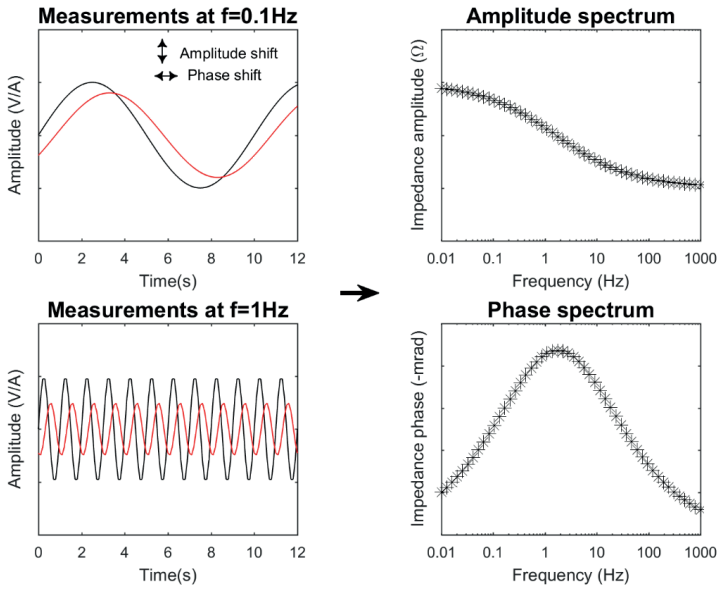

Figure 2.1. Left: Examples of current waveforms and potential readings used for FD IP measurements. Right: Principle of the collection of a FD IP spectrum.

Figure 2.2 also show a close-up on different off-time voltage decays, commonly referred to as IP decays. The IP decay is traditionally quantified as chargeability, which is a measure of the integrated mean value below the potential curve. The integrated mean value can be performed for an arbitrary time window and is therefore highly influenced by measurement settings (e.g. the length of the on- and off-time periods and the noise-content in the data). Another way of quantifying the magnitude of the IP decay is to use the intrinsic chargeability, defined as follows by Seigel (1959):

$$m_0 = \frac{V_s}{V_p} \qquad 2.2$$

In Equation 2.2, V_p is the primary potential during the late current on-time and V_s is the secondary potential, i.e. the level to which the potential drops immediately after the interruption of the current (see Figure 2.2). Although not equally as intuitive as with FD measurements, the shape of the TD IP decays also contains spectral information. Figure

2.2 shows examples of three different decays where the intrinsic chargeability is constant, but the relaxation processes occur over different time periods, characterized by the relaxation time τ.

Measurements of the SIP-effect with FD or TD systems are theoretically equivalent, as TD data can be transformed to FD and vice versa via the Fourier transform (e.g. Sumner, 1976). However, the actual spectral content of TD data depends on data acquisition parameters such as the sampling rate and time duration of the current pulses and there are few studies available in the scientific literature showing experimental equivalence of FD- and TD SIP measurements.

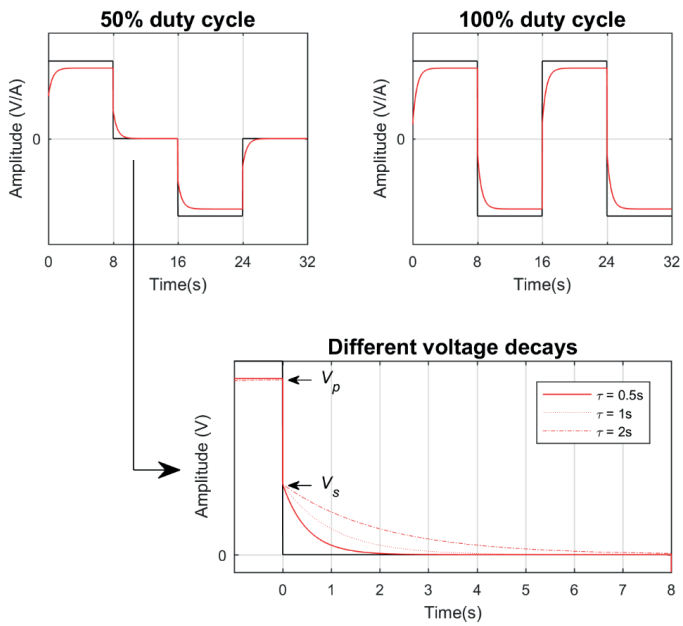

Figure 2.2. Top: Examples of current waveforms and potential readings used for TD IP measurements. Bottom: Illlustration of spectral information contained in measured voltage decays with different relaxation times.

2.2 The Cole-Cole model

For the interpretation of IP frequency spectra or time decays it is common to fit a phenomenological model to the data. In this way, a number of parameters can be extracted, which describe the shape of the spectrum or decay. The most commonly used model, the Cole-Cole model, assumes the existence of a relaxation peak on the frequency (or time) axis. The Cole-Cole model was originally developed for the dielectric permittivity dispersion of polar liquids (Cole and Cole, 1941) and was later adopted to describe the impedance of geological materials by Pelton *et al.* (1978):

$$Z^*(\omega) = R_0 \left[1 - m_0 \left(1 - \frac{1}{1+(i\omega\tau)^c}\right)\right] \quad 2.3$$

where $Z^*(\omega)$ is the complex impedance as a function of angular frequency ω, R_0 is the low-frequency resistance and m_0, τ and c are the Cole-Cole parameters. The intrinsic chargeability, m_0 (defined in Equation 2.2 above) is a measure of the strength of the polarization, while the relaxation time τ and the frequency exponent c describe the position and width of the peak on the frequency axis. c can take values between 0 and 1 and a wider range of particle sizes in the material results in lower values of c and a broader peak. The Cole-Cole model expressed in terms of complex resistivity $\rho^*(\omega)$ or complex conductivity $\sigma^*(\omega)$ has the following forms (Tarasov and Titov, 2013):

$$\rho^*(\omega) = \rho_0 \left[1 - m_0 \left(1 - \frac{1}{1+(i\omega\tau_\rho)^c}\right)\right] \quad 2.4$$

$$\sigma^*(\omega) = \sigma_0 \left[1 + \frac{m_0}{1-m_0} \left(1 - \frac{1}{1+(i\omega\tau_\sigma)^c}\right)\right] \quad 2.5$$

where ρ_0 and σ_0 are the low-frequency resistivity and conductivity, respectively. The subscripts of the relaxation time, τ_ρ and τ_σ, are used to denote the fact that the relaxation time is not exactly the same in Equations 2.4 and 2.5; Tarasov and Titov (2013) showed that Pelton's impedance model and the corresponding complex resistivity model (Equations 2.3 and 2.4) actually deviates slightly from a true Cole-Cole model as defined by Cole and Cole (1941).

In addition to the Cole-Cole model there are also other, less common phenomenological models that can be used to fit and interpret SIP data. Variants of the Cole-Cole model are the Cole-Davidson model and the generalized Cole-Cole model (Nordsiek and Weller, 2008) which assumes and allows, respectively, asymmetrical peaks in the spectra. The Debye model, from which the Cole-Cole model was developed, represent the relaxation of a single particle size and is equivalent to the Cole-Cole model with a c value of 1 (Cole and Cole, 1941). An approach based on the superposition of several Debye models, referred to as the Debye Decomposition, was introduced by Nordsiek and Weller (2008). This approach is not limited to the assumption of a single relaxation peak in the data and has, thus, the advantage of allowing a larger flexibility in the spectral shapes. Other means

of fitting data with e.g. several relaxation peaks is to use multiple Cole-Cole models (Pelton *et al.*, 1978).

It is important to note that not all IP frequency spectra or time decays have shapes with single or multiple relaxation peaks. Other common shapes are e.g. spectra where the phase angle increase with frequency or is constant and independent of frequency. For the latter case, Constant Phase Angle (CPA) models can be used to describe the data. A relatively common variant of the CPA model is the Drake model introduced by Van Voorhis *et al.* (1973).

3. PHYSICAL MECHANISMS

SIP research spans over several disciplines including electromagnetism, electrochemistry, geology, petrophysics and groundwater chemistry. A few generally accepted mechanisms are used in the literature to conceptually, analytically or numerically explain the varying spectral responses observed between different materials. Experimental work has also yielded many well-established empirical or qualitative relationships between SIP responses and a variety of sample properties. This chapter gives a brief review of these previous findings, together with a summary about how SIP-effects are believed to arise in geological materials and why spectral dispersions are observed.

3.1 The SIP phenomenon

When an electric current of current density **J** (A/m^2) is transmitted through a material, an electric field **E** (V/m) arise and charges in the material start to move in an attempt to balance the potential gradients. The material property describing the movement of charges is the electrical conductivity, σ (S/m):

$$\boldsymbol{J} = \sigma \boldsymbol{E} \tag{3.1}$$

In geological materials, there are three main processes that influence the ability of the material to conduct current; ionic conduction though the pore water, surface conduction along mineral surfaces and electronic conduction within the solid minerals. The ionic conduction is dominant and takes place in the pore spaces of the materials, while the electronic conduction usually is neglible since most geological materials act as electrical insulators.

The surface conduction arises since ions are attached to grain surfaces in contact with pore water electrolytes. These ions are electrostatically and/or chemically attracted from the electrolyte in the inner so-called fixed (Stern) layer. Additional electrostatically attracted ions form the outer, diffuse layer. Both layers are collectively called the Electrical Double Layer, EDL (Bard and Faulkner, 2001).

The existence of EDLs around grain surfaces is also one of the most basic physical explanations of the electrical polarization in geological materials. As a potential gradient develops in the material, ions attached in the EDL are displaced accordingly which is measured as a phase delay in FD or as a lingering potential after a current pulse in TD. The theory of this mechanism, referred to as the electrochemical polarization mechanism, was first described by Schwarz (1962) and later treated by other authors (de Lima and Sharma, 1992; Lesmes and Morgan, 2001; Leroy *et al.*, 2008; Revil and Florsch, 2010). There seems to be a general agreement that it is mainly the fixed layer of the EDL that is responsible for the polarization (de Lima and Sharma, 1992; Lesmes and Morgan, 2001), while the diffuse layer is believed to be interconnected over the grain boundaries and

therefore only contributes to surface conduction (Leroy *et al.*, 2008; Revil and Florsch, 2010). The grain size distribution is considered as the main geometrical control on the spectral dispersion in the electrochemical polarization mechanism.

If electrically conducting mineral grains, e.g. iron sulfides, are present in the material, an additional polarization process is active. This process involves charge transfer across the mineral interface. With potential gradients across the material, the rate of the redox reactions change from being in equilibrium to becoming dependent on the diffusion rate of active ions species to and from the surfaces. If the diffusion rate is higher than the reaction rate, excessive ions are depleted on the mineral surface. The faradic (redox processes) and non-faradic (e.g. the electrochemical polarization mechanism) processes together cause a measureable impedance in materials containing conductive minerals (Sumner, 1976; Wong, 1979; Ward, 1988; Bard and Faulkner, 2001). This polarization mechanism is called electrode polarization (from electrochemical terminology) and is usually much stronger in magnitude compared to polarization mechanisms active in materials with insulating mineral grains.

In materials with electrically non-conducting mineral grains, there is, in addition to the electrochemical polarization, also another mechanism that can be active. This mechanism is the membrane polarization mechanism, which was first formulated by Marshall and Madden (1959). The membrane polarization mechanism is based on the concept of alternating ion-selective and non-selective zones in the geological material. Ion-selective zones are passages in the pore network with different ion transparency for cations and anions. For example, Vinegar and Waxman (1984) considered ion-selective zones as clay-rich zones with high negative surface charge, which would block the anion flow (due to electrostatic repulsion) while cations pass through unaffected. This leads to series of ion surplus and ion deficiency in the non-selective zones, and thus a net polarization of the material (Marshall and Madden, 1959; Vinegar and Waxman, 1984). The strength of the membrane polarization effect is dependent on the length ratio between the non-selective to ion-selective zones (Marshall and Madden, 1959). In the Marshall and Madden (1959) model, the relaxation time increases with the length of the non-selective zone in relation to the ion-selective zone. Titov *et al.* (2002) presented a special case of the membrane polarization model for sands, the so-called small narrow pore model (SNP). In this case, the ion-selective zones consist of short and narrow pores where the EDLs of the pores cause different ion transparencies. In the SNP model, the relaxation time is proportional to the length of the ion-selective zones (Titov *et al.*, 2002). Recently, Bücker and Hördt (2013a) proposed a modified version of the SNP model together with a long narrow pore (LNP) model valid for the case of long narrow ion-selective zones. According to these results, there are two different relaxation regimes, where the relaxation behavior differs between the SNP and LNP geometries. The main geometric control on the spectral dispersion is the (distribution of) length of the ion-selective zones (SNP model) or non-selective zones (LNP model). Bücker and Hördt (2013b) incorporated also pore radii properties in the membrane polarization model, which also might affect the spectral dispersion. In all versions of the membrane polarization model, the existence of

alternating series of ion-selective and non-selective zones is a prerequisite for electrical polarization.

In addition to electrical conduction (Equation 3.1), electrical fields also interact with materials by electric displacement of charge, $\boldsymbol{D}$ **(**C/m^2**).** The material property describing the electric displacement field is the dielectric permittivity, ε (F/m):

$$\boldsymbol{D} = \varepsilon \boldsymbol{E} \tag{3.2}$$

The dielectric permittivity can be described as a property determining the ability of the material to obtain an intrinsic (or physical, as opposed to chemical) polarization. For example, a conductor usually has a low dielectric permittivity while materials of polar molecules (e.g. water) can obtain high intrinsic polarization. Measurements of either one of the complex properties (electric conductivity or dielectric permittivity) also involves measurements of the other; they cannot be separated in the potential field. The total measured effect can be quantified by either the complex conductivity $\sigma^*(\omega)$ or the complex permittivity $\varepsilon^*(\omega)$, which are related as follows (e.g. de Lima and Sharma, 1992):

$$\sigma^*(\omega) = \mathrm{i}\omega\varepsilon^*(\omega) \tag{3.3}$$

or

$$\sigma'(\omega) + i\sigma''(\omega) = -\varepsilon''(\omega) + i\omega\varepsilon'(\omega) \tag{3.4}$$

This relationship means that when the imaginary part of the complex conductivity is measured, the real part of the dielectric permittivity is also measured simultaneously. The influence of the latter becomes increasingly important as the measurement frequency (ω) increases. Therefore, the imaginary conductivity spectra measured with SIP do not only contain chemical polarization effects described by the polarization mechanisms above (electrode-, electrochemical- or membrane), but also effects from physical polarization of the sample materials, determined by their real dielectric permittivity. The complex dielectric permittivity of composite (e.g. porous) materials can be described with effective medium mixing models, e.g. the Bruggeman-Hanai-Sen equation (Sen *et al.*, 1981; Lesmes and Morgan, 2001):

$$\varepsilon^* = \varepsilon_w^* \theta^m \left(\frac{1-\varepsilon_m^*/\varepsilon_w^*}{1-\varepsilon_m^*/\varepsilon^*}\right)^m \tag{3.5}$$

where θ is the porosity, m is the Archie cementation exponent (Archie, 1942), ε^*, ε_w^* and ε_m^* are the complex permittivity of the composite material, pore fluid and mineral grains, respectively. At low frequencies, Equation 3.5 reduces to Archie's law and a corresponding DC equation for the dielectric permittivity (Sen *et al.*, 1981; Lesmes and Morgan, 2001).

The impedance of Equation 3.5. is caused by the so-called Maxwell-Wagner effect, which is a physical polarization mechanism that occur at interfaces between different materials in a composite medium (e.g. Beek, 1960; Iwamoto, 2012). The relaxation of Equation 3.5 occurs in the MHz to GHz-range according to calculations in Sen *et al.* (1981). In the SIP field, effective medium mixing models such as Equation 3.5 are used together with electrochemical polarization models to calculate the total complex conductivity response at high frequencies (e.g. de Lima and Sharma, 1992; Lesmes and Morgan, 2001), also referred to as the Maxwell-Wagner effect. This interfacial polarization effect, caused by pore fluid ion accumulations at interfaces between different materials, is generally considered relevant at frequencies above ~1kHz (Kemna *et al.*, 2012).

3.2 SIP and material properties

A comprehensive amount of systematic laboratory research investigating links between SIP and different material properties exist. It is not possible to give a representative review here, but some of the main findings from previous work will be summarized. If not stated otherwise, the relationships referred to below have been found from research on sandstones or unconsolidated sandy materials.

Many studies have shown that the grain size distribution have an important control on the SIP response of the material, both in terms of polarization magnitude and spectral dispersion. Larger proportions of finer materials (silt and clay) in sandy materials generally leads to increased polarization, as quantified by the imaginary conductivity (Slater and Lesmes, 2002; Slater and Glaser, 2003). The explanation is that smaller grains have larger specific surface areas compared to larger gains, and therefore more attached charges per unit volume. Since clay minerals have flat structures and high surface charge densities, the clay content of materials has a particular importance for the polarization strength of the material (Vinegar and Waxman, 1984; Slater and Lesmes, 2002). The petrophysical property specific surface area to pore volume (S_{por}) is one of the most important material properties controlling the polarization of a sandy materials (Weller *et al.*, 2010, 2015; Weller and Slater, 2015).

In SIP spectra with polarization peaks, the grain size distribution control the relaxation time and the width of the peak. The dominant grain- or pore throat size in the material control the polarization length scale, and therefore the relaxation time (Scott and Barker, 2003; Binley *et al.*, 2005; Kruschwitz *et al.*, 2010; Zisser *et al.*, 2010). Kruschwitz *et al.* (2010) observed an exception to this trend for tight sandstones with a significant proportion of very small pores. For these rocks, the small pores seem to act as connected diffusion paths which leads to larger relaxation times than expected (Kruschwitz *et al.*, 2010). Others have also found variations that are dependent on structural characteristics of the material. For example, denser packing of grains tends to lead to a domination of smaller pore throats and shorter relaxation times than would otherwise be expected for the actual dominant grain size in the material (Scott and Barker, 2003; Koch *et al.*, 2011).

In some materials, multiple relaxation peaks can occur due to e.g. effects of grain surface roughness (Nordsiek and Weller, 2008; Leroy *et al.*, 2008). It is also known that relaxation peaks are not always present in SIP spectra. In unconsolidated sediments or weakly consolidated sandstones, spectra can be observed where the imaginary conductivity increase with frequency in a power-law type of shape (Slater and Glaser, 2003).

In addition to geometrical and structural material properties, the strength of the SIP response is also dependent on groundwater conditions, e.g. salinity. The imaginary conductivity generally increases with salinity until a plateau is reached at relatively high salinities, where after it starts to decrease with further increase of the salinity (Slater and Glaser, 2003; Weller and Slater, 2012). The water saturation is also known to affect the polarization magnitude (Titov *et al.*, 2002; Slater and Glaser, 2003; Ulrich and Slater, 2004) as well as the relaxation time (Binley *et al.*, 2005).

According to Slater and Glaser (2003), lithological properties are significantly more important in controlling the variation of imaginary conductivity compared to fluid conductivity and saturation. Similarly, groundwater salinity variations are of second order importance for controlling the relaxation time (Kruschwitz *et al.*, 2010). In contrast, any presence of conductive minerals, e.g. sulphides, have a major effects on the polarization of a material (see e.g. Pelton *et al.*, 1978; Slater *et al.*, 2006; Nordsiek and Weller, 2008).

4. METHODS

As the main aim of the work is to investigate SIP parameters from TD IP tomography, this is also the main method. Other important methods are FD SIP laboratory measurements as well as different methods for the characterization of microstructures and chemical content of relevant materials. The methods for microstructure characterization include x-ray tomography and image analysis as well as production of thin sections analysed with optical microscopy or Scanning Electron Microscopy (SEM). Energy Dispersive x-ray spectroscopy (EDS) and x-ray fluorescence (XRF) are methods that have been used for measurements of the chemical composition in samples.

The overall methodological approach has been to interpret inverted spectral TD IP data conceptually in light of the generally accepted theoretical mechanisms of the spectral IP response (chapter 3). The focus has been to consider the effect of varying microgeometrical structures on the SIP mechanism and resulting spectral shapes. Microstructures differing from the conceptual spherical grains described by most mechanistic IP models are likely to have important effects on the resulting inverted SIP parameters. This is the case especially at the type of applications investigated in this work (e.g. limestone environments), but in general, subsurface material structures can be expected to vary greatly also at many other types of field sites. Therefore, investigations of the microstructure of the studied materials and interpretation in light of the results has been an important part of this work.

The need to support interpretations of TD SIP field data with FD SIP laboratory measurements has increased during the course of the work. To include both types of measurements in this work has been an overall methodological approach to gain a better understanding of how spectral parameters from TD IP field data relate to the comprehensive amount of relationships that exist between material properties and FD IP spectra.

4.1 Time domain spectral IP tomography

The TD IP tomography data in this work was measured with 2D layouts, standard electrode configurations (pole-dipole and multiple gradient protocols) and collection of full-waveform data with the Terrameter LS instrument. The instrument settings have changed over the course of the work, as new insights as well as developments of data processing methods and inversion software have progressed.

The data in the appended Johansson *et al.* (2015) and Johansson *et al.* (2016) were acquired with a 50% duty cycle waveform with 1s pulses, 10ms delay time and 1000Hz sampling frequency. In Johansson *et al.* (2015), the IP decays were integrated over multiples of 60ms to supress noise from electric power- and train traffic noise with frequencies 50Hz and 16 2/3Hz, respectively. The gating resulted in 8 logarithmically

spaced time windows, see Table 4.1. For Johansson *et al.* (2016), the recent signal processing scheme of Olsson *et al.* (2016) was used, which removes periodic noise from the data. With this approach, the data could be re-gated without integration over 60ms and earlier time windows could be retrieved. The data were gated with 1ms delay time in 20 logarithmically spaced time windows, see Table 4.1.

For Johansson *et al.* (2019b), the data were collected using a 100% duty cycle (Olsson *et al.*, 2015). A pulse length of 8s and a sampling frequency of 3750Hz were used to retrieve a wide spectral range. The data were preprocessed with the above mentioned processing scheme and the decays were gated in 39 logarithmically spaced time windows (Table 4.1).

Table 4.1 Time ranges of the TD IP data used in different parts of this work. The different time ranges is a result of different data acquisition settings and processing methods.

Paper	Time windows, center gate times (ms)
Johansson *et al.* (2015)	40, 100, 160, 220, 310, 460, 640, 970
Johansson *et al.* (2016)	1.5, 3.5, 4.5, 5.5, 7, 9.5, 13, 17.5, 24, 33, 45.5, 63, 83, 113, 163, 223, 313, 433, 583, 823
Johansson *et al.* (2019b)	1.13, 1.39, 1.79, 2.32, 2.85, 3.51, 4.44, 5.64, 7.10, 8.97, 11.4, 14.3, 17.9, 22.4, 28.2, 35.5, 44.8, 56.5, 71.2, 89.3, 109, 139, 179, 229, 289, 349, 439, 559, 709, 889, 1100, 1370, 1730, 2210, 2810, 3560, 4490, 5660, 7130

After gating of the IP decays, all data were manually processed in Aarhus Workbench (Auken *et al.*, 2009). An important part of this work has been to evaluate the quality of the acquired apparent potential decays. Corrupted decays, outliers, individual noise affected gates or early time gates affected by inductive coupling were removed from the datasets. The processed data were then inverted in 2D with AarhusInv (Fiandaca *et al.*, 2013; Auken *et al.*, 2014).

Due to the limited spectral range of the data used in *Johansson et al.* (2015), it was considered difficult to resolve the Cole-Cole parameters in a reliable way. Therefore, most of the inversions were instead carried out with a CPA model parameterization (Van Voorhis *et al.*, 1973), yielding inverted sections of resistivity and phase angle distributions. Motivated by the increased spectral range of the data in Johansson *et al.* (2016), all inversions were performed with the standard Cole-Cole parameterization (Pelton *et al.*, 1978). This parameterization results in four sections showing the distributions of resistivity, chargeability, relaxation time and frequency exponent. By that time, depth of investigation (DOI) estimates were also provided by AarhusInv (Fiandaca *et al.*, 2015) giving a measure of how reliably the Cole-Cole parameters were resolved by the inversions.

Later, new Cole-Cole parameterizations of the model space were added to AarhusInv; the Maximum Phase Angle (MPA) and Maximum Imaginary Conductivity (MIC) parameterizations (Fiandaca *et al.*, 2018). Instead of inverting for the chargeability in Equations 2.4 or 2.5, the maximum phase angle or imaginary conductivity, corresponding to the location of the relaxation peak, is extracted during the inversions. In addition to being more easily interpreted, the MPA and MIC parameterizations improve the DOI due to reduced parameter correlations (Fiandaca *et al.*, 2018). In Johansson *et al.* (2019b), the data were inverted with the MIC Cole-Cole parameterization in order to enhance the comparison of the inverted parameters with laboratory FD IP spectra.

In order to analyse and translate spectral ranges acquired with TD IP waveforms to FD IP parameters, the discrete Fourier transform was used to perform a spectral analysis of synthetic TD IP data (Johansson et al., 2020).

4.2 Frequency domain spectral IP measurements

Two different kinds of sample holders for FD SIP measurements were designed as a part of this work. For Johansson *et al.* (2019a), special sample holders were designed for an experiment combining SIP measurements and high-resolution x-ray tomography on PCE contaminated sand samples. Since PCE is chemically aggressive, the cylindrical sample holders needed to be manufactured from glass. Small diameters of the sample holders (2cm) were chosen to enable high-resolution x-ray tomography over the entire sample volume between the potential electrodes at reasonable time scales. The lengths and locations of the potential electrode channels followed the geometrical recommendations given by Zimmermann *et al.* (2008). A photograph of the sample holder is shown to the left in Figure 4.1. Current plate electrodes manufactured from stainless steel were placed at each end of the cylindrical sample holder, inside the screw caps visible in Figure 4.1.

The FD SIP measurements in Johansson *et al.* (2019a) were carried out with a ZWL-SIP04 impedance meter (Zimmermann *et al.*, 2008). Prior to the experiments, numerous test measurements were performed to ensure good data quality with the sample holders. These tests included measurements on electrolyte filled sample holders with different potential electrode materials, degree of potential electrode retraction from the current path as well as contact material between the electrodes and samples (water, porous discs and agar-agar gel of different viscosity). Furthermore, numerous test measurements were carried out with different sand types, grain size distributions and electrolyte conductivity. For each sample type, several replicas were prepared and measured. The contact resistances of all electrodes were controlled qualitatively with a multimeter. The extensive amount of test measurements resulted in high confidence in the quality of the data with the final experimental setup. In this setup, drilled rubber lids containing retracted copper wire electrodes were used as potential electrodes. Agar-agar gel was prepared from the same electrolyte as was used in the sample, pushed into the rubber lids where it became solid and worked as a contact medium between the electrodes and the

sample. The quality of each potential electrode preparation was controlled with SIP measurements on pure electrolyte.

A different kind of sample holder was designed for the measurements on the limestone core samples in Johansson *et al.* (2019b). The core pieces were vacuum-sealed in plastic bags during the drilling to preserve the natural groundwater in the samples. In the laboratory, the FD SIP spectra of each core sample was measured immediately after it was unpacked. Therefore, flexible sample holders with adjustable electrodes were designed which enabled SIP measurements on cores with different lengths. The sample holders, shown to the right in Figure 4.1, consist of plate current electrodes of stainless steel placed on both ends of the cylindrical sample and adjustable half-ring potential electrodes, also manufactured from stainless steel. The core rests on the potential electrodes, and the current electrodes are fixed to the sample with a clamp. Watersoaked textile were used between the electrodes and the sample to decrease contact resistances. The contact resistances were controlled qualitatively with a multimeter.

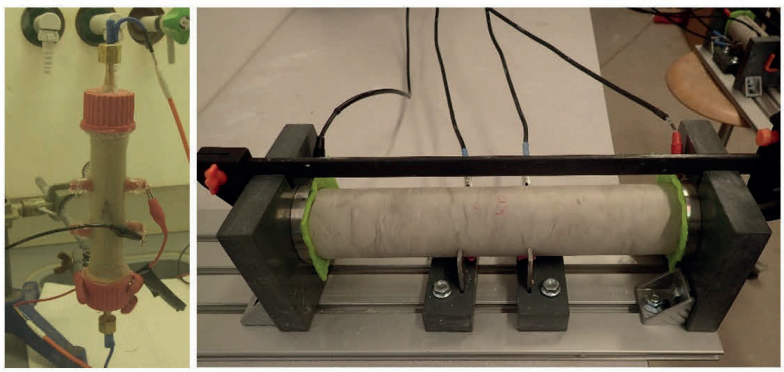

Figure 4.1. Left: Photograph of the sample holder used for SIP experiments with NAPL contaminated sand in Johansson *et al.* (2019a). Right: Photograph of the experimental setup used for SIP measurements on limestone cores in Johansson *et al.* (2019b).

The FD SIP measurements on the core samples in Johansson *et al.* (2019b) were performed with an Ontash PSIP instrument (Version 1.3.1i-2). For obvious reasons, data quality tests on pure electrolytes or replica measurements could not be performed with this experimental setup. However, at least two of the core samples could be considered as replica samples due to their close similarities in physical, chemical and lithological properties. The fact that the SIP responses of these samples were nearly identical is an indication that data of adequate quality for our purposes were obtained with this experimental setup.

4.3 NAPL geometry in sand: x-ray transmission tomography and image analysis

There are many factors that affect the SIP response of NAPL contaminated soils. In addition to the properties of the geological and biological materials present at a field site, the chemical properties and degradation status of the NAPLs are also important. In addition, NAPL dissolution into the groundwater and alteration of groundwater chemical properties also affects the electrical response of the soil. In this work, focus has been on the altered microgeometrical structure in the pore space by the presence of free-phase NAPLs in sands. This is motivated by the fact that the field- and laboratory measurements in this work were performed on sands (or sandy materials) contaminated with the DNAPL tetrachloroethylene (PCE). This specific chemical is non-polar and electrically insulating and has low solubility in water. Therefore, it often exists as an own phase in the pore system over long time periods, and the insulating nature makes the electrical behaviour, in some aspects, comparable to electrically isolating sand grains.

The TD IP tomography results from a PCE contaminated field site in Johansson *et al.* (2015) were compared to borehole data of contaminant concentrations and geological materials. Since the comparison alone did not give a better understanding of the TD IP response, a comprehensive literature review of SIP research on NAPL contaminated materials was performed. The results and data interpretations of previous research were, however, ambiguous and variable. A theoretical discussion of the expected electrical response (according to the electrochemical and membrane polarization mechanisms) of different geometrical configurations of free-phase NAPL in the pore space of sands was therefore presented in Johansson *et al.* (2015). This discussion resulted in different hypotheses of varying SIP responses for different NAPL configurations, which aided the interpretation of the field data and could provide a possible explanation to why different behaviours have been observed in different laboratory studies of NAPL contaminated samples.

The theoretical findings in Johansson *et al.* (2015) resulted in a need to test the hypothesis of geometrical controls on the SIP response experimentally. In order to do so, x-ray transmission tomography and image analysis were used in Johansson *et al.* (2019a) to investigate the real NAPL distribution in sand samples visually and quantitatively. In x-ray transmission tomography, the sample is exposed to x-rays that are attenuated through the sample and collected at a detector screen, resulting in radiographs. During a 180° rotation of the sample, several radiographs are collected from different angles, and the set of radiographs are reconstructed to a 3D volume of the attenuation properties of the sample. The reconstructed data consist of an image stack with a specific pixel (voxel) resolution (that depends on the data acquisition settings), where the intensity in the images is proportional to the x-ray attenuation coefficient the materials in the sample. In this work, a laboratory based x-ray transmission tomography setup (Zeiss Xradia XRM520 at Lund University) was used, and the voxel resolution of the images in Johansson *et al.* (2019a) were 13-15 μm.

In order to perform a quantitative analysis, the images were filtered from noise and transformed to binary images with the grains, water, air or PCE phase segmented out. The class segmentation was performed using histogram based intensity thresholds. A 3D watershed segmentation was also performed on the grain binary images in order to label each grain with a unique number. This enabled quantification of properties such as grain- and PCE blob size- and volume distributions, total PCE content, porosity and water saturation. All calculations of properties were based on counting the number of pixels and scaling by the voxel resolution.

4.4 Microstructure of limestones: carbonate texture, thin sections, SEM and EDS-anaysis

Limestones are interesting geological materials in the sense that they vary considerably in composition. Since the calcium carbonate originate from fossils, the shapes of the grains vary and depend on the fauna during the time of deposition. Limestones have been deposited over long time periods over which both fauna and depositional environment varied. Factors such as shallow or deep water conditions and ocean stream directions affects the amount of siliciclastic material, e.g. clay content, in the limestone as well as structural patterns of limestone layers. In this work, three different groups of limestone have been investigated with SIP. Microscopic thin section studies were, together with other methods, used to aid the field data interpretations in Johansson *et al.* (2016) and Johansson *et al.* (2019b). The carbonate textures of samples were obtained from the point counting method (Flügel, 2010) according to the Dunham classification system (Dunham, 1962).

In addition to the carbonate texture, chemical mapping of samples from the Kristianstad basin were performed in Johansson *et al.* (2016). The chemical mapping was motivated by the documented significant amount of siliciclasic material and abundance of glauconite layers and pyrite in the limestone (Kornfält *et al.*, 1978). Drill cutting samples were obtained from an entrepreneur drilling in the Kristianstad basin and the samples were examined with SEM and EDS-analysis. SEM is a technique for high-resolution 2D characterization of the sample surface topography. An electron probe is used to scan the sample and secondary emitted or back-scattered electrons from the sample surface are detected. The contrast in images collected with a secondary electron (SE) detector is mainly caused by an uneven sample surface. A backscattered electron (BSE) detector can gain additional information since the signal strength of backscattered electrons is dependent on the mean atomic number in the sample. The EDS detector acquires spectra of characteristic x-rays emitted from the sample during the electron interactions, i.e. chemical information. In Johansson *et al.* (2016), the drill cutting samples were mounted on glass plates with carbon tape and carbon coated in a vacuum evaporator (Cressington Carbon Coater 108carbon/A). Thereafter, they were investigated with a SEM with SE, BSE and EDS detectors (Hitachi S-3400N with an Oxford instruments Inca X-sight EDS-

detector). The BSE detector was used to scan the samples for high density minerals where after the spectra were analyzed with EDS. The procedure gave an indication of the chemical composition and the mineral content in the samples, and based on these results, three core levels were selected for thin section manufacturing. Chemical mappings of the thin sections were then performed with EDS-analysis. These results gave information about both structural and mineralogical content in the limestone samples.

In the Limhamn quarry (Johansson *et al.* (2019b)), a core drilling was performed along one of the measurement profiles after the TD SIP tomography. Core samples were investigated in laboratory with FD SIP, and bulk properties (water content and density) were measured before the cores were cut along the length axis and documented with photography. Representative thin sections were thereafter produced, from which the carbonate textures were obtained. The chemical content of the samples were estimated with XRF measurements on powder samples.

5. RESULTS AND DISCUSSION

In this chapter, the main results and conclusions of this work are summarized and discussed. The first two sections present and discuss results which are relevant in order to justify comparisons between SIP data from TD and FD methods as well as laboratory and field conditions. General methodological differences and remaining possible pitfalls are also discussed. This is followed by two chapters that present main results and conclusions related to the two different application areas investigated in this work.

5.1 FD spectral resolution of TD IP waveforms

A signal sampled in TD can be analyzed in FD via the discrete Fourier transform. Figures 5.1 and 5.2 show results from the discrete Fourier transform of synthetic TD IP waveforms with acquisition settings representing those used in this work. The potential waveforms have been modelled as Debye relaxations with 4mV/V chargeability and 0.1s relaxation time (the frequency exponent c is 1). As can be seen in Figures 5.1 and 5.2, the square waveform is composed of linearly spaced sinusoids with frequencies corresponding to the odd harmonics of the square wave fundamental frequency. The longer period of the square waveform used for Johansson *et al.* (2019b) (Figure 5.2) compared to Johansson *et al.* (2015) and Johansson *et al.* (2016) (Figure 5.1) results in more densely spaced frequencies and a lower frequency limit in the FD. Furthermore, the higher sampling frequency results in data resolved at higher frequencies in FD. These results illustrate that the data acquisition settings used for TD IP tomography have a great impact on the spectral resolution of the data in FD.

In some earlier research studies, it has been stated that the spectral range of TD IP waveforms is always narrow because the fundamental frequency dominate over the higher harmonics (Soininen, 1984; Kemna, 2000). However, limited spectral ranges in previous work is mainly a consequence of limited data acquisition parameters and/or analytical analysis methods. For example, the discrete Fourier transforms of TD IP data in Van Voorhis *et al.* (1973) resulted in narrow FD spectral ranges due to factors related to the data acquisition and analytical analysis methods; the sampling frequency of the data was below 72Hz and only five harmonics of the Fourier series were used for the FD evaluation.

In Johansson et al. (2020) variations of the modelled potential waveform relaxation time showed that, for TD IP data sampled at 3750 Hz, Debye relaxations with relaxation times at least down to 0.001s could be well resolved in FD. When the relaxation time was further decreased, the FD IP representation of the data started to become increasingly distorted due to aliasing effects in the FD. Spectral analysis of noise contaminated TD waveforms were also presented in Johansson et al. (2020), and it was shown that processing with e.g. low pass filters prior to the spectral analysis improve the resolution of the data in FD.

Also Fiandaca (2018) showed that TD current waveforms measured with high sampling frequency contain information at high frequencies. This information is, however, only present at early decay times (Fiandaca, 2018). This means that even if the measured

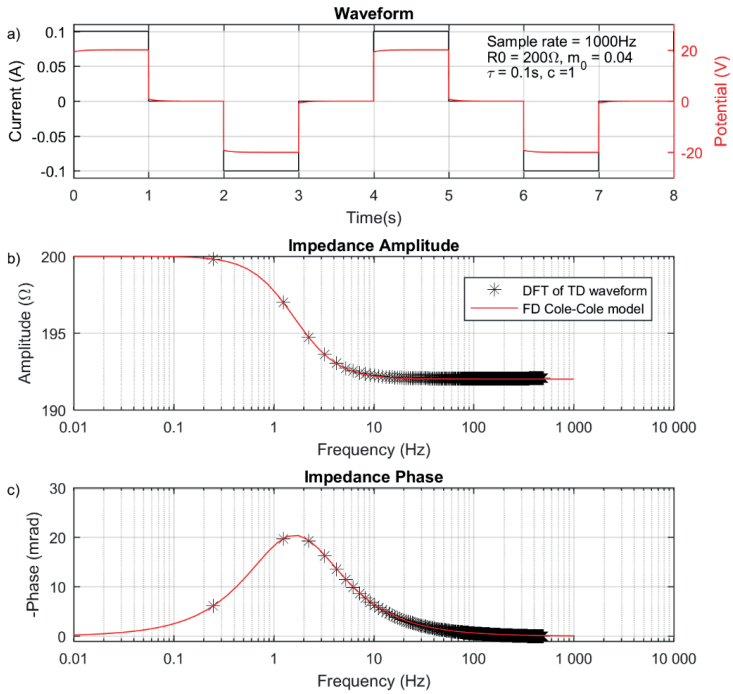

Figure 5.1. a) Synthetic current waveform with 50% duty cycle and potential sampling with 1000Hz sampling rate. The potential decay is modelled as a Debye relaxation with a chargeability of 4mV/V and a relaxation time of 0.1s. b-c) Impedance amplitude and phase of the discrete Fourier transform of the TD waveforms in a. The red lines show the FD Debye model in the frequency range 0.01-1000Hz.

TD IP data contain the full spectrum of frequencies shown in Figures 5.1 and 5.2, the processing of the data can reduce the spectral content, especially at high frequencies. To preserve as much high-frequency information as possible, the delay time should therefore be minimized when IP decays are gated. The delay times in this work range from 10ms (Johansson *et al.*, 2015) to 1 ms (Johansson *et al.,* 2016 and Johansson *et al.,* 2019b). This can be compared to delay times of e.g. 40ms in a previous study where difficulties of resolving certain combinations of Cole-Cole parameters from IP decays were encountered (Tombs, 1981). Other early studies have, however, reported successful recovery of Cole-

Cole parameters despite using IP decays with delay times of 30-40ms (Johnson, 1984; Vanhala, 1992) or even 100ms (Lewis, 1985).

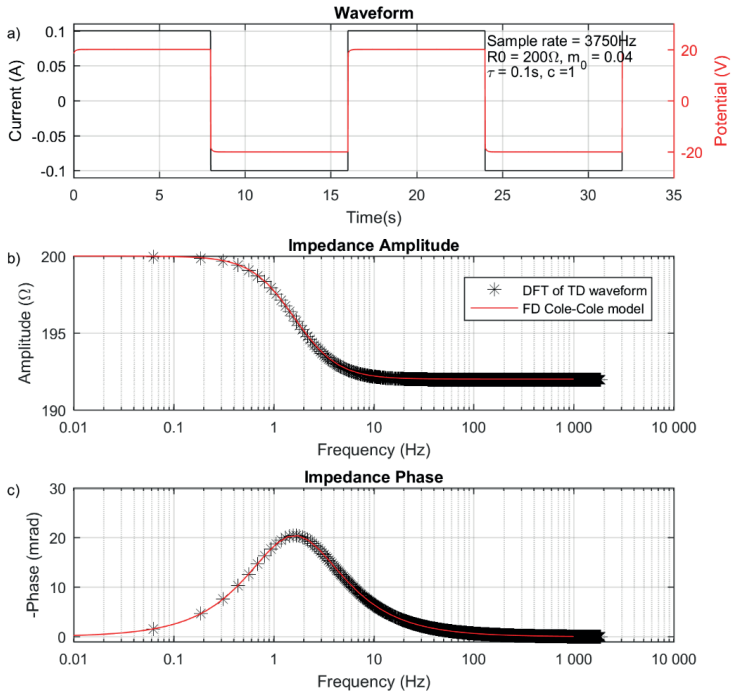

Figure 5.2. a) Synthetic current waveform with 100% duty cycle and potential sampling with 3750Hz sampling rate. The potential decay is modelled as a Debye relaxation with a chargeability of 4mV/V and a relaxation time of 0.1s. b-c) Impedance amplitude and phase of the discrete Fourier transform of the TD waveforms in a. The red lines show the FD Debye model in the frequency range 0.01-1000Hz.

In addition to the delay time, the time range of the IP decay is also of importance for the ability to recover spectral parameters. The relaxation time can be larger than the decay time and still resolved with the Cole-Cole model (Johnson, 1984). However, long current pulses are favorable also because they can improve correct estimations of all Cole-Cole parameters from IP decays, according to Madsen *et al.* (2017).

In summary, discrete Fourier transforms can be used to show the spectral content of acquired TD IP data in FD IP form. Although mostly used for synthetic data in this work, the method can also be used to compare real TD IP and FD IP data. With modern instruments and appropriate data acquisition settings, the TD IP spectral range is comparable to spectral ranges commonly used for FD SIP measurements. The full spectral range of acquired TD IP data is, however, reduced by necessary processing steps

if spectral parameters are extracted from IP decays with e.g. the Cole-Cole model. The possibilities to correctly resolve Cole-Cole parameters from IP decay spectra is thus dependent on both the acquired spectral range and the data processing. The need for data processing is, in turn, dependent on the level of noise and electromagnetic coupling in the data. However, the usable spectral range of FD IP data is also affected by noise and electromagnetic coupling. In that sense, there are no major differences between the measurement methods.

5.2 Laboratory and field SIP measurements

In the appended Johansson *et al.* (2019b), inverted Cole-Cole parameters from TD IP tomography were directly compared to FD IP spectra measured on samples. The samples originated from a core that was drilled after the TD IP tomography in the central part of the measurement line (see Figure 5.8 below). The natural groundwater was preserved in the core samples, but the temperature difference between the field and laboratory conditions was around 15±2°C. Figure 5.3. show the results of the comparison. The inverted Cole-Cole values from the model cells closest to the core location were used in Equation 2.5 to visualize the TD IP spectra. The comparison is only relevant for low frequencies since the parameterization used in the inversion software assumes a spectral shape with a single relaxation peak. Therefore, the inverted TD SIP results do not consider the increase in imaginary conductivity that is often observed at higher frequencies, e.g. in the Cole-Cole shaped spectra from samples P5 and P6 in Figure 5.3.

Another main difference between the laboratory spectra and the inverted values in Figure 5.3 is that the inverted cell values are affected by inversion constraints and decrease in resolution with increasing depth. The cell values also represent much larger volumes than the core samples, especially at deeper levels. It is therefore not obvious how to compare the different methods to each other. Nevertheless, at comparable depths below the ground surface, the inverted cell values are generally in the same order of magnitude as the FD IP spectra. The general trend of decreasing real- and imaginary conductivity values with depth below the ground surface is represented also in the inverted model cell values. In the inverted cell at level 3.4-4.5m (bold blue line in Figure 5.3b), the shape of the imaginary conductivity spectra and the relaxation time match the laboratory FD IP spectra of the shallowest core samples P1 and P2 very well. At levels 16.0-22.4m (red bold lines), the inverted relaxation time values are somewhere in between the values measured at samples P5 and P6 (assuming that the latter has a relaxation time outside the frequency range, as indicated by the spectral shape).

The overall conclusion of the comparison is that the inverted Cole-Cole parameters from the TD IP tomography data are comparable to FD IP spectra measured on laboratory cores. Therefore, these results indicate that relationships established between FD SIP and rock properties in laboratory research can be used for interpretation of data measured at the field scale. Interpretation of inverted field data should, of course, always be made in

general terms representative of the expected precision of the inverted data values. This applies to both spectral IP parameters, integral chargeability and resistivity.

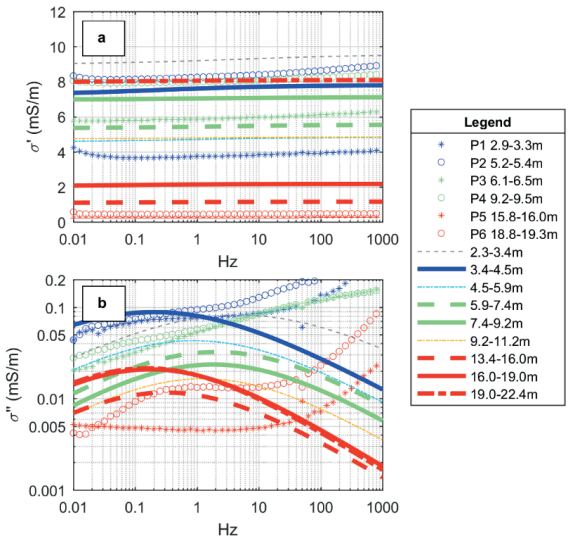

Figure 5.3. Direct comparison of FD IP spectra measured at limestone cores and inverted TD IP Cole-Cole parameters from the closest model cells.

Some pitfalls with the interpretation of inverted spectral parameters from field scale TD IP tomography remain. A main issue is that at a natural field site, the material might give rise to many different and overlapping spectral shapes. In Figure 5.3b, the spectral shapes of samples P3 and P4 are not Cole-Cole shaped. Still, the inversion software parameterization assumes Cole-Cole shaped spectra in all model cells. The results in Figure 5.3b indicate that inverted Cole-Cole shaped spectra are obtained also for materials with spectral shapes increasing with frequency (although it cannot be ruled out that the inverted results represent average material properties in the large volumes represented by the model cells). The Cole-Cole model cannot take any shape that would represent this spectral shape. Inverted Cole-Cole parameters from TD IP tomography might therefore in some cases not represent the material properties well. However, if varying spectral shapes is a large issue within a TD IP data set, this problem would be revealed from the average inversion model misfit value. It is also possible to visually inspect the fit between individual data decays and their corresponding forward model response. Therefore, general trends in inverted Cole-Cole parameters (as those presented in Johansson *et al.*, 2019b) can be considered reliable.

It is clear that the acquired high-frequency information is not fully utilized with Cole-Cole inversions of TD IP data, unless the Cole-Cole relaxations occur at relatively high frequencies. An approach with e.g. double Cole-Cole parameterization in the inversion

software or a single Cole-Cole relaxation overlapped with a high-frequency permittivity response would potentially solve this issue.

5.3 Application: NAPL contaminated soil

The main results of Johansson *et al.* (2015) consist of a review and a theoretical discussion about how different NAPL configurations in sands are expected to affect measured SIP responses (in terms of Cole-Cole parameters). Four conceptual models of residual NAPL configurations were used as a basis for the discussions, see Figure 5.4. In all cases, the conceptual models were compared to the case of a non-contaminated and water-saturated sand. Since NAPLs in general are high-resistive chemicals, increased bulk resistivity was expected for all possible NAPL geometries.

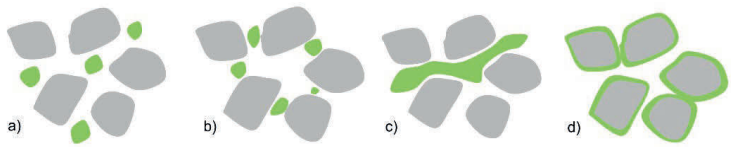

Figure 5.4. Conceptual models of geometrical configuration in NAPL contaminated sand.

In the conceptual models depicted in Figures 5.4a and 5.4b, the residual NAPL phase is trapped in pores or pore throats. These geometries were expected to result in increased polarization magnitude and decreased relaxation time according to the electrochemical polarization mechanism. This result is based on the likely assumption that EDLs form around NAPL surfaces. Increased polarization magnitude is expected since the total surface area in the sample increase, at the same time as a larger proportion of the current is forced to move through EDLs instead of the pore water. Simultaneously, the dominant particle size in the system likely decreases with NAPL droplets smaller than the average grain, which leads to decreased relaxation time.

Also when the membrane polarization mechanism was considered, the polarization magnitude was expected to increase for the geometries in Figure 5.4a and 5.4b. In this case, the main reason would be a larger difference in ion-transparency between the ion-selective and non-selective zones. It was assumed that the ion-selective zones would shift location from pore throats to pores for the case in Figure 5.4a, in analogy with the theoretical concept of unsaturated sands in Titov *et al.* (2004). The increase in non-selective zone length in relation to ion-selective zone length could lead to increased relaxation times (Marshall and Madden, 1959). For the geometry in Figure 5.4b, however, no change in relaxation time was expected since the length of the ion-selective and non-selective zones would remain the same as for clean sand.

In Figure 5.4c, the NAPL phase is interconnected between several pores and pore throats. With this geometrical structure, the electrochemical polarization magnitude likely decreases compared to a clean sand. The reason is that the EDL of the NAPL phase might short-circuit the polarization of neighbouring grains when both the diffuse and the fixed layers are interconnected. In terms of the membrane polarization mechanism, the alternating series of ion-selective and non-selective zones would vanish. In contrast to the conceptual models in Figures 5.4a and 5.4b, the NAPL configuration in Figure 5.4c was not expected to change the dominant length scale in the sand and, thus, neither the relaxation time.

The NAPL phase can potentially also coat grain surfaces as illustrated in Figure 5.4d. In this case, the specific surface area of the NAPL coated grains decreases and their EDLs are disabled. The relative strengths of the grain and NAPL EDLs will affect whether the electrochemical polarization magnitude increase or decrease. Either way, the increased particle sizes would likely lead to longer relaxation times compared to the case of a clean sand. For this conceptual model, it is interesting to note that the expected relaxation time response could potentially differ between the electrochemical and membrane polarization mechanisms. It can be argued that the length ratio between the non-selective pores and the ion-selective pore throats decrease as an effect of the NAPL films around the grains. According to the Marshall & Madden model, a reduced length ratio would lead to decreased relaxation times (Marshall and Madden, 1959).

In addition to the different conceptual models in Figure 5.4, the case of a fully NAPL saturated pore space was also briefly discussed in Johansson *et al.* (2015). Under such circumstances, it was assumed that the NAPL would suppress the electrochemical and membrane polarization mechanisms otherwise present in a clean sand.

The inverted results of the TD IP tomography showed two well-limited phase anomalies within in the sandy till material. A high resistive anomaly appeared at another location, roughly in between the two phase anomalies. The drilling data did not indicate any significant variations in geological material, and the resistivity and phase responses were relatively homogeneous except for the abovementioned anomalies. With the results of the theoretical considerations of different residual NAPL configurations, a likely interpretation of the field data could be presented. It was assumed that the high PCE concentrations in the source area likely leads to a NAPL configuration similar to Figure 5.4c, i.e. NAPL phase extending across several pores and pore throats. Since decreased polarization magnitude can be expected for this geometry, the absence of a phase anomaly at the location of the source area could be explained (the background polarization of the sandy till was already low; below ~1mrad or, expressed as normalized phase angle, below ~0.04mS/m). Instead, the phase anomalies were found at locations around the edges of the contamination source area, where the chemical sampling indicated intermediate PCE concentrations. The increased phase values (and normalized phase values) at these locations were interpreted as a possible result of a NAPL configuration similar to Figure 5.4a, where ongoing biodegradation might have fractionated formerly more continuous

NAPL phase. There are, of course, also numerous other factors at a field site that could explain increased phase values in a degradation zone, such as bacterial growth, iron precipitation from bacterial activity or locally altered groundwater chemistry (Abdel Aal *et al.*, 2006; Atekwana and Slater, 2009). These factors were, however, unknown at the field site.

The theoretical discussions of the different conceptual NAPL configurations in Johansson *et al.* (2015) largely enhanced the interpretation of the field data and could possibly, at least partly, explain why contradictory results between different research studies have been observed previously. However, the NAPL configurations in Figure 5.4 are simplified and conceptual models of reality, and it is probable that a combination of several NAPL configurations are present in real samples or field conditions. Furthermore, the actual SIP response of the different NAPL geometries needs to be verified experimentally. The main aim of Johansson *et al.* (2019a) was, therefore, to test the hypotheses in Johansson *et al.* (2015) of NAPL geometrical controls on the SIP response of sand samples.

In the experiments in Johansson *et al.* (2019a), one clean and two PCE contaminated sand samples (referred to as PCE1 and PCE2) were investigated with SIP and x-ray tomography. Preparation of NAPL contaminated samples is a challenging process, and it is difficult to predict the actual NAPL distribution achieved in the samples. In this study, the manual mixing method was used, as this is the most common method used in previous similar studies of the SIP response of NAPL contaminated samples. The x-ray tomography results, shown in Figure 5.5, revealed that the PCE concentration differed (as expected) between the two contaminated samples. Image analysis was used to quantify bulk properties of the three samples. The results, shown in Table 5.1, showed that much lower PCE concentrations (1.5% and 11% of the pore space) than expected (10% and 40% of the pore space) were actually achieved with the manual mixing method.

Image analysis was also used to quantify the volume distribution of the PCE blobs in PCE1 and PCE2. The PCE volumes were significantly smaller in PCE1 compared to PCE2, although ~60% of the blobs had volumes larger than the average gain volume. In PCE2, the corresponding number was ~92%. Around 41% of the total amount of PCE in sample PCE2 was interconnected in three large blobs. These results verify what was already indicated by the 3D-visualisations in Figure 5.5, i.e. that a large part of the PCE is interconnected over several pores in PCE2 while it is mainly arranged as isolated blobs in PCE1.The SIP measurement results from the three samples are shown in Figure 5.6. For both contaminated samples, the real conductivity values increased with PCE contamination while the phase- and imaginary conductivity responses decreased.

It is, however, likely that the reason behind this electrical response is different in PCE1 and PCE2. In PCE2, the NAPL distribution reminded of a combination of the conceptual models in Figures 5.4c and 5.4d, i.e. NAPL interconnected over several pores and pore throats or NAPL coating grains. Decreased phase- and imaginary conductivity responses are in agreement with the hypotheses regarding these NAPL configurations in Johansson

et al. (2015). Although the expected resistivity response of these configurations was not thoroughly discussed in Johansson *et al.* (2015), the increased real conductivity values measured at PCE2 were unexpected. These experimental results indicate that the EDLs of the PCE phase might be stronger (and contribute with stronger surface conduction) than expected in Johansson *et al.* (2015). Recent modelling results from Bücker *et al.* (2017) support this interpretation. They found that with high NAPL zeta potential, the insulating effect of the NAPL phase displacing electrolyte in the pore space was overridden by increased surface conduction.

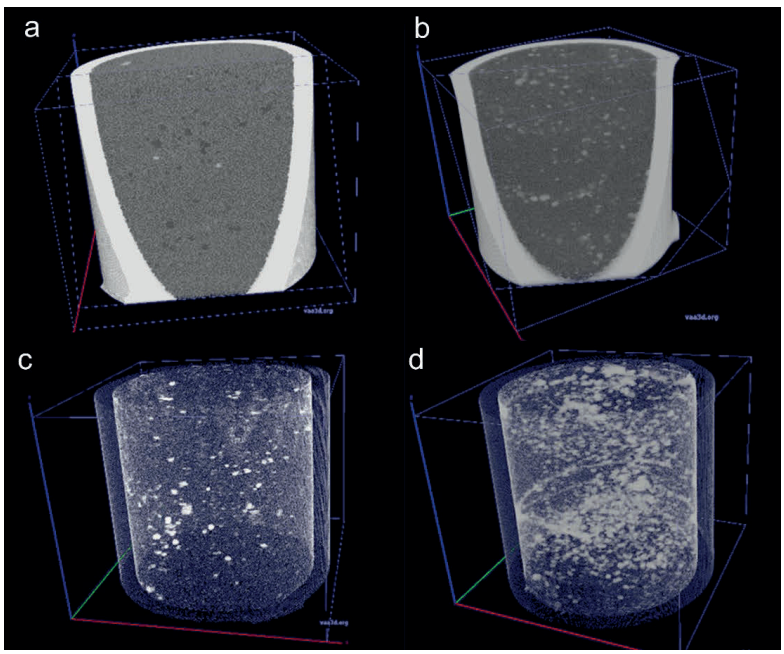

Figure 5.5. 3D-views of x-ray transmission tomography results showing the distribution of PCE in two contaminated sand samples. a) sand sample with a PCE concentration of 1.5% of the pore space (PCE1). Grains are visualized with gray color, water and air with darker shades of gray and PCE with light color. b) sand sample with a PCE concentration of 11% of the pore space (PCE2). c) transparent view of PCE1 which shows that the PCE is mainly distributed as isolated blobs. d) transparent view of PCE2 which shows that large parts of the PCE is interconnected through the pore space.

The electrical response of sample PCE1 was interpreted as an effect of several factors. The relatively high porosity of PCE1 could partly explain the increased real conductivity compared to the clean sand according to calculations in Johansson *et al.* (2019a) with Archie's law (Archie, 1942). The decreased phase- and imaginary conductivity responses

were interpreted as an effect of larger porosity and/or presence of PCE- and air bubbles with smaller specific surface areas than the average sand grains. The NAPL geometry in PCE1 did not directly resemble any of the conceptual models in Figure 5.4, except that grains were occasionally coated with PCE as in Figure 5.4d. It can, however, be argued that the SIP results of PCE1 seem to be in agreement with the hypothesis about the NAPL geometry in Figure5.4a. In Figure 5.4a, the NAPL droplets are smaller than the grains but in PCE1, the droplets were instead generally larger than the grains (an effect of the sample preparation method). Instead of leading to increased electrochemical polarization due to increased specific surface areas in the sample, the cause of the reduction of polarization could be decreased specific surface areas in PCE1.

Double Cole-Cole models fitted to the data in Figure 5.6 indicated a slight increase in relaxation time for PCE1 and a slight decrease in PCE2. These charges are, however, very small and probably not significant. If the decrease in relaxation observed in PCE2 would be considered real, however, the result might be an indication that membrane polarization effects dominate the spectral response of sample PCE2 (according to the discussion of the conceptual models in Figures 5.4c and 5.4d above).

Table 5.1 Sample properties obtained from image analysis of the x-ray tomography results.

	Clean	PCE1	PCE2
Porosity (%)	37	44	40
Water content (%)	63	41	35
PCE (% of pore space)		1.5	11
Air (% of pore space)		4.4	1.2
Water (% of pore space)		94.1	87.8

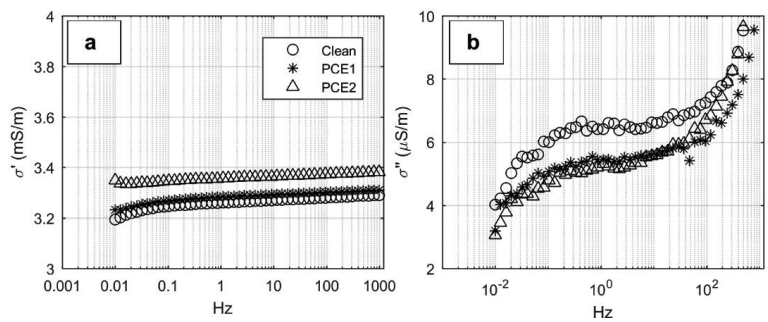

Figure 5.6. FD IP spectra measured on the clean- and PCE contaminated samples. The results show that the real conductivity values increased while the imaginary conductivity values decreased in the contaminated samples.

5.4 Application: Lithological variations in limestones

The TD IP tomography data from the Kristianstad basin in Johansson *et al.* (2016) showed a relatively large variation in inverted Cole-Cole parameters. Figure 5.7 shows the inverted Cole-Cole sections from one of the measurement lines, located in a rural area where the noise levels in the data were relatively low (the other measurement lines in Johansson *et al.* (2016) were measured in an urban area with disturbances from both electromagnetic noise, installations, roads and buildings). Figure 5.7e shows the normalized Cole-Cole chargeability, a parameter that is qualitatively comparable to the imaginary conductivity (Slater and Lesmes, 2002b), i.e. more closely related to lithological properties than the chargeability in Figure 5.7b. The normalized chargeability section (Figure 5.7e) indicates zones of elevated polarization, and the two most shallow of these zones seem to correspond to lower resistivity values (Figure 5.7a). A different pattern can be observed for the relaxation time (Figure 5.7c). Most prominent is a zone of low relaxation times (~0.05-0.1s), but there are also zones of slightly elevated relaxation times in the bottom of the section as well as close to the surface in the northwestern part.

No reference data from the same location were available to aid the interpretation of these variations. However, microgeometrical properties of the limestone in two other core drillings from the Kristianstad basin were used to investigate possible sources to the observed SIP variations. In one of these cores, located approximately 1-2km from the site where the data in Figure 5.7 were measured, lithological data were available from the literature (Kornfält *et al.*, 1978). These data showed that the carbonate texture and mineral content varied with depth. It is also known that the grain sizes of the carbonate texture and presence of other mineral constituents generally vary dramatically in the Kristianstad basin, both vertically and horizontally. The reason is varying depositional environments with both marine periods and subaerial periods (Christensen, 1984).

A detailed microgeometrical investigation of limestone material from another core drilling was performed in Johansson *et al.* (2016). The results showed that the carbonate texture varied between two closely spaced core levels. The carbonate grains were of approximately the same size (sand-sized) in both samples, and both samples could be classified as grainstones or packstones. However, variations in fossil assemblage and grain shapes were observed between the different levels. Furthermore, the SEM and EDS-analysis revealed presence of pyrite grains and glauconitic feldspar grains in the deeper of the two analysed samples.

Based on the microgeometrical studies, possible sources for the observed variations in Figure 5.7 were suggested. Zones of elevated normalized chargeability could possibly be related to lithological zones with locally higher presence of clay minerals, pyrite or glauconitic minerals. Different relaxation times could reflect variations in fossil composition and grain shape (e.g. relative abundance of enlongated fossils). The proportion of cement and micritic matrix in the carbonate texture was also suggested as

possible explanations to the observed variations. It was concluded that the variation in Cole-Cole parameters likely indicates textural variations within the limestone, but also that more research is needed to directly relate different microgeometrical properties to SIP responses in limestones.

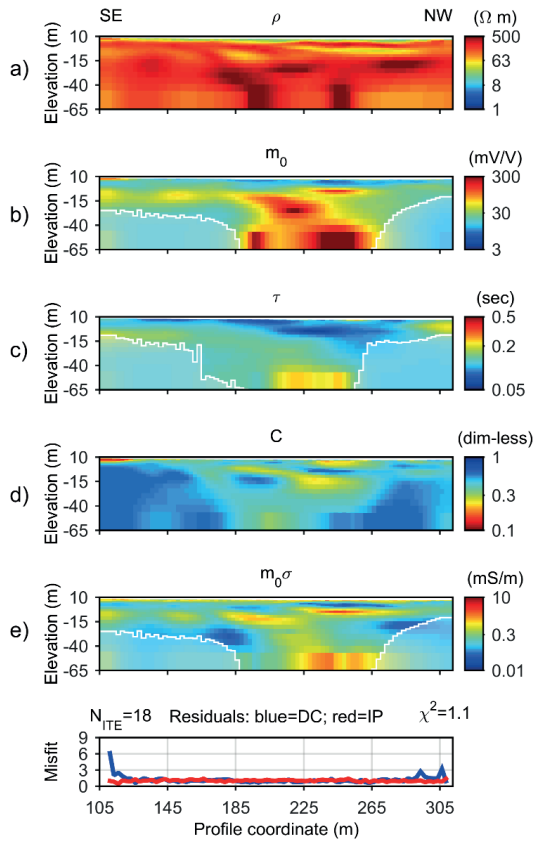

Figure 5.7. Inverted TD SIP tomography data from the Cretaceous limestone environment in the Kristianstad basin.

One of the aims of Johansson *et al.* (2019b) was therefore to carry out an attempt to directly relate inverted Cole-Cole parameters to variations in microstructures and composition of limestones. A TD IP tomography survey was performed in the Limhamn quarry, followed by a core drilling along one of the measurement lines. Figure 5.8 shows a 3D-view of the inverted measurement results. Note that the conductivity (in mS/m) is shown in Figure 5.8a and not the resistivity as in Figure 5.7a. In Figure 5.8a, the dramatic

shift in conductivity (marked with a bold dashed line) corresponds to the boundary (K-Pg boundary) between the Cretaceous (Maastrichtian Stage) and the Paleogene (Danian Stage) limestone. The laboratory analyses of the core showed that the carbonate texture is very different below and above this boundary. In the Cretaceous limestone, the carbonate texture is classified as calcareous mudstone and the proportion of fine-grained matrix is ~90% or above. The Paleogene limestone is generally coarser and more lithified. The Paleogene carbonate textures mainly consist of wackestones (~25-30% carbonate grains), but also packstones and grainstones (~55-60% carbonate grains) are present among the samples. These large textural differences explain the dramatic shift in conductivity values across the K-Pg boundary in Figure 5.8a. The very low conductivity above the K-Pg boundary in Figure 5.8a corresponds to a lithological unit with four prominent chert beds and/or anomously dense limestone (detected by optical and acoustic logging of the borehole).

Figures 5.8b-d show the inverted Cole-Cole parameters. The calculated DOI threshold was shallower for these parameters compared to the conductivity. Therefore, the visualized sections in Figures 5.8b-d only represent the Paleogene limestone. The Paleogene limestone in the Limhamn quarry corresponds to the Danian stage and was deposited in carbonate mounds at the ancient sea floor. The lowermost dashed line in the relaxation time section, Figure 5.8c, corresponds with the expected elevation of the boundary between the lower and middle Danian. The geometry of this interface also corresponds to the typical height and wavelength of the carbonate mounds in the Limhamn quarry. The shift towards longer relaxation times in the deeper part of the section is likely related to a difference in fossil grain shape distribution between the middle and lower Danian. The lower Danian is dominated by enlongated cylindrical bryozoan fragments, which could explain the long measured relaxation times. In the upper Danian, the limestone also contains coralline fossils and the fauna is generally characterized by a larger biodiversity, i.e. a larger variety of fossil shapes. Zones with shorter relaxation times and elevated imaginary conductivity (Figure 5.8b) were interpreted as a consequence of larger variation in the grain shapes and microstructure of the middle Danian limestone.

Figure 5.9 show results of FD SIP measurements on samples from the core (note the different scales between the Paleogene samples in Figure 5.9a-c and the Cretaceous samples in Figure 5.9d-f). In agreement with the TD IP tomography data in Figure 5.8a, the real conductivity values in Figures 5.9a and 5.9d differ significantly between the Paleogene and the Cretaceous limestone. Figure 5.9b and 5.9e show that the shapes of the phase spectra are more variable in the Paleogene limestone compared to the Cretaceous. In the Cretaceous samples, the phase spectra are generally characterized by low values at low frequencies and increasing phase values towards higher frequencies. The only exception is the SIP spectrum of sample C3, which is characterized by high amounts of siliciclastic clay minerals and a laminated structure at the macro scale. The SIP spectrum was measured perpendicular to the bedding, and this sample has the highest values of phase and imaginary conductivity of all samples in this study.

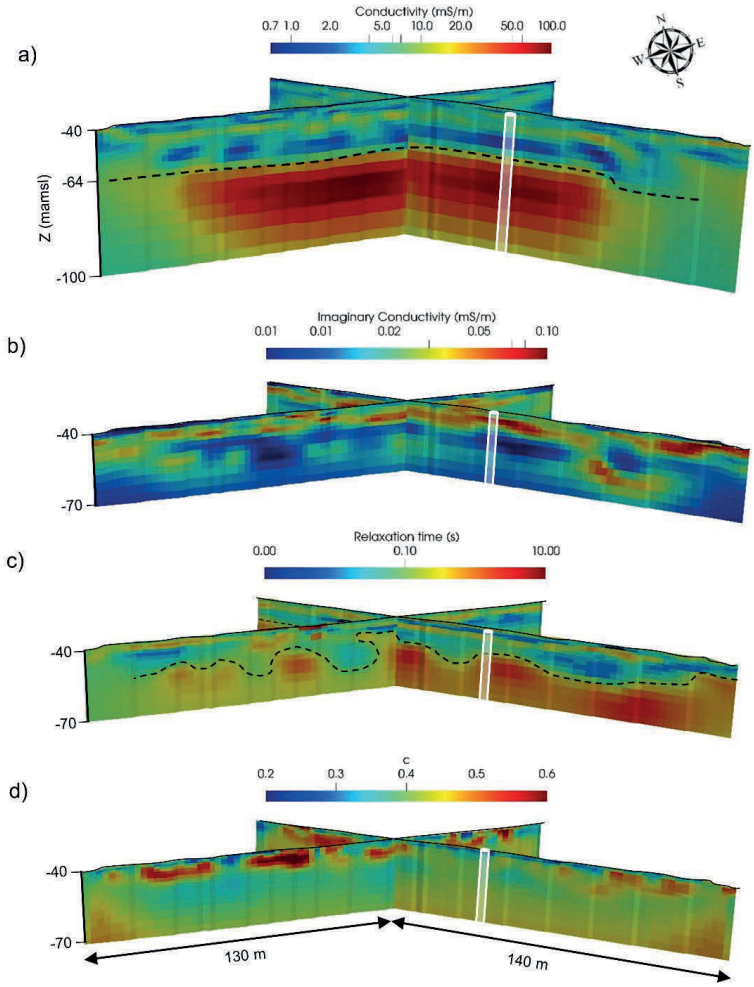

Figure 5.8. 3D-views of inverted TD SIP tomography results measured in the Limhamn quarry.

The imaginary conductivity spectra of the Paleogene samples in Figure 5.9c show a pattern that seems consistent with depositional depth. The magnitudes and shapes of the shallowest samples P1 and P2 are similar, as are the magnitudes and shapes of the following samples P3 and P4. Samples P5 and P6 are located in the aforementioned zone with chert beds and dense limestone, which is also reflected by the extremely low conductivity values in Figure 5.9a. In the Cretaceous limestone, a similar pattern in the

imaginary conductivity data can be observed at some levels (Figure 5.9e). Here, the shallowest samples C1 and C2 have similar spectra, as does the deeper samples C4 and C5.

In total three different types of limestones have been investigated in this work and their main characteristics are compared in Table 5.2. Timewise, the investigated materials range from Upper Cretaceous, Santon Stage to Lower Paleogene, Danian stage. The carbonate textures vary from calcareous mudstones to grainstones. The Cretaceous limestone samples from the Kristianstad basin generally contained significantly larger amounts of calcite cement and silisiclastic minerals compared to the Paleogene and Cretaceous samples from the Limhamn quarry. These variations mainly have their origin in the history of the depositional environments. In the Paleogene limestone in the Limhamn quarry, the conductivity of the grainstones, packstones and wackestones varied in a range of ~1-10mS/m, which is approximately the same range as was measured at the Cretaceous grainstones and packstones in the Kristianstad basin. Due to the different inversion parameterizations used in Johansson *et al.* (2016) and Johansson *et al.* (2019b), the relative polarization magnitudes between the sites cannot be compared accurately. However, the data indicate that the relaxation time of the polarization generally seem to be lower in the Cretaceous limestone of the Kristianstad basin compared to the Paleogene limestone in the Limhamn quarry. This might reflect the large abundance of cylindrical bryozoan fragments in the limestone from the Limhamn quarry.

Table 5.2 Summary of the characteristics of the different types of limestones investigated in this work.

Location	Geological Series, Stage and Formation	General lithological description	Main carbonate texture of samples
Kristianstad basin	Upper Cretaceous, Santon, Campan and lower Maastrichan Stages	Well consolidated limestone with ~70-80% calcium carbonate. Layers with glauconitic sand and mudmatrix occur, flint and chert uncommon (Kornfält *et al.*, 1978)	Grainstones/packstones, >50% grains, 20-30% cement (Johansson *et al.,* 2016)
Limhamn quarry	Upper Cretaceous, Maastrichan Stage, Höllviken formation	Very fine-grained chalk with few macro fossils, siliciclastic clayish layers and flint occur (Brotzen, 1959)	Mudstones, <15% grains, 0% cement (Johansson *et al.,* 2019b)
Limhamn quarry	Lower Paleogene, Danian stage (Limhamnsledet), Höllviken formation	Bioherm structures dominated by bryozoan macrofossils and coralls, ~96-99% calcium carbonate (Sivhed *et al.*, 1999)	Wackestones and packstones/grainstones, 25-60% grains, 0-15% cement (Johansson *et al.,* 2019b)

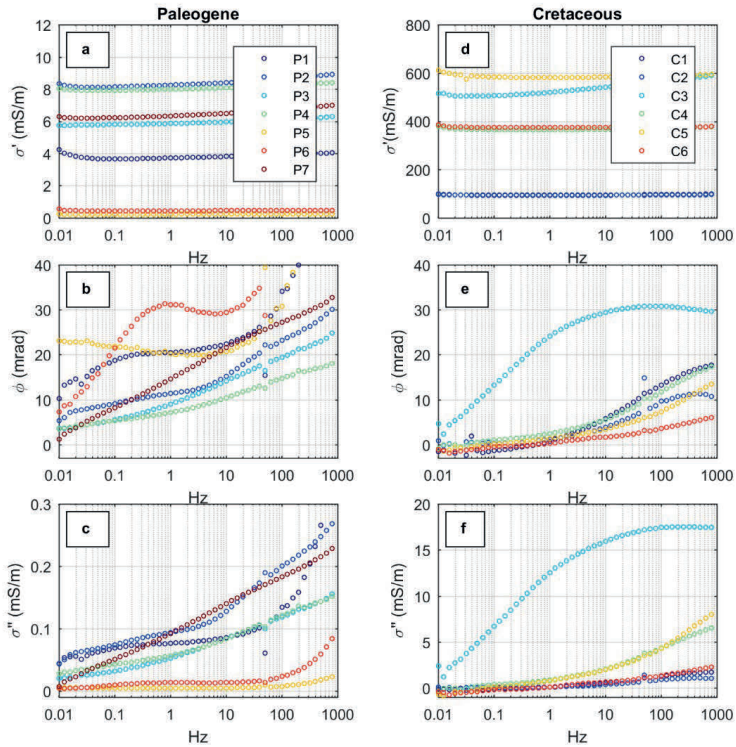

Figure 5.9. FD SIP results measured on core samples from the Limhamn quarry.

6. CONCLUSIONS

A main conclusion of this work is that inverted spectral IP parameters from field TD IP tomography are comparable to FD IP spectra on laboratory samples (Johansson *et al.*, 2019b). A prerequisite for this statement is that high quality TD IP data have been measured with appropriate settings, e.g. high sampling frequency and preferably long current pulses (Johansson (in revision)). Furthermore, the data needs to be processed in a systematic and as far as possible objective manner and inverted with an appropriate parameterization of the SIP response. The results from Johansson *et al.* (2019b) showed that under these circumstances, relationships between SIP responses and lithological properties measured on sample cores can be generalized at the field scale with the use of Cole-Cole parameters. When larger data coverage, i.e. faster measurements, are preferred over spectral resolution, the TD IP data can be approximated by inversion with a CPA parameterization (Johansson *et al.*, 2015). However, depending on the spectral resolution actually obtained after processing as well as the expected polarization length scales in the investigated material, Cole-Cole parameters might be successfully extracted also from data measured with relatively short current pulses (Johansson *et al.*,2019a).

Regarding interpretation of inverted SIP parameters, e.g. Cole-Cole parameters, an important conclusion is that an understanding of the expected microstructural geometry of the studied materials, and variations thereof within the study area, is essential. This often involves engagement with other research fields, for example chemistry and multiphase fluid flow (Johansson *et al.*, 2015 and Johansson *et al.*, 2019a) or sedimentology (Johansson *et al.*, 2016 and Johansson *et al.*, 2019b). All data interpretations in this work are based on generally accepted theoretical models of the SIP phenomenon in homogeneous granular materials. The microgeometrical structures of real materials have been investigated theoretically or experimentally, whereafter the results have been reduced to a simplified but representative conceptual model.

The investigations of NAPL contaminated sands at different scales ranging from microstructure via laboratory SIP measurements to field TD IP tomography have potentially increased the general understanding of the electrical response of NAPL contaminated sites. The attempt in this work to isolate the geometrical effects of the SIP response has led to the conclusion that different SIP responses can be expected depending on the geometrical nature of the contamination. The concentration of the contaminant in the pore space seems to play a large role. High concentrations increase the likelihood of an interconnected NAPL phase, for which a decrease in polarization magnitude can be expected. In zones with lower concentrations, e.g. the fringes around a source zone or geological layers through which DNAPLs have migrated, increased polarization (and potentially shorter relaxation times) might be detected as a result of NAPLs trapped in pores and pore spaces.

A methodological conclusion related to the work with NAPL contaminated sands is that it is difficult to interpret SIP data without knowing the achieved NAPL distribution.

Absence of geometrical data might at least partly explain why results from previous research studies have pointed in different directions. Combined use of SIP, x-ray tomography and image analysis is a promising approach to increase the understanding of the SIP responses of NAPL contaminated materials.

The results from this thesis demonstrate the value of spectral inversion of IP data in large-scale field surveys. In the data measured in limestone environments, the patterns in the Cole-Cole sections often deviate largely from the resistivity- and chargeability or imaginary conductivity distributions. For example, the possible carbonate mound structures would not be detected without spectral inversion of the field data; these structures were only visible in the relaxation time section.

Limestone materials have not attracted much attention in previous SIP research. The results from this work show that limestones can give rise to a large variety of SIP responses. The main cause of the variations in all spectral parameters is that the mineral composition, carbonate texture and microstructure vary largely within limestone materials. In order to understand inverted spectral parameters from TD IP tomography data measured in limestone environments, it is therefore important to investigate, at least, the main mineral- and fossil constituents of the formation in question. Dominant fossil shapes and depositional structures is also important knowledge for interpretation of inverted SIP parameters.

One of the main objectives of this work has been to investigate and highlight the effect of different microgeometrical patterns on the SIP response. Interpretation of SIP responses in light of the microgeometric structure of materials has therefore been a theme throughout this work. This approach has improved the quality of the data interpretations significantly. A general conclusion is that large variations in inverted spectral parameters at the field scale are likely related to geometrical variations at the microscale, at least at the type of field sites encountered here. Despite scale differences between laboratory and field conditions, the distribution of Cole-Cole parameters can give information on large-scale differences in material structures.

The second main objective has been to narrow the current gap between FD laboratory SIP research and field scale TD SIP tomography surveys. In this work, the physical equivalence of FD and TD SIP measurements have been demonstrated together with an emphasis on the importance of appropriate data acquisition settings and processing. The results of this work also shows that the physical understanding of the SIP phenomenon gained through laboratory work can be used to understand inverted spectral parameters from field scale TD IP tomography. Scale barriers between both methods remain, although results from this work shows that the inverted Cole-Cole parameters were of the same order of magnitude as values from SIP measurements on laboratory samples.

7. OUTLOOK

The results and conclusions of this work is a step towards a better understanding of inverted parameters from spectral TD IP tomography. Within specific application areas, further research is needed on material microstructures and corresponding SIP responses. Such research can potentially also increase the general understanding of the SIP phenomenon. More comprehensive research needs, some of which might narrow the gap between field- and laboratory scale SIP research further, have also been identified and are presented below.

7.1 Electrochemical characterization of materials

The SIP research field is closely related to the electrochemical research field. This is especially apparent in mechanistic models of polarization mechanisms. Electrochemical- and membrane polarization models often require an extensive amount of electrochemical surface parameters. At the same time, electrochemical measurements of these properties in geological materials seem rare. In future work, it could therefore be beneficial for the research field if more electrochemical studies of different e.g. mineral- and NAPL surfaces were available. Such research could improve both the usefulness of existing mechanistic models and the general understanding of the SIP responses in different materials.

7.2 Numerical modelling of geometrical effects

The results in this work showed that the combined use of x-ray tomography and image analysis is a promising approach to achieve a better understanding of the effects of geometrical variations on the SIP response of samples. In future work, the use of x-ray tomography could be extended to SIP research of other material types. Furthermore, the geometry obtained from high-resolution x-ray tomography can be meshed and imported into softwares for numerical modelling. With appropriate material properties, SIP measurements can be simulated numerically and compared to measured SIP results. With such an approach, the need for homogeneous samples to understand the SIP response is reduced and geometrical variations of geological materials, e.g. anisotropy, can be investigated systematically.

7.3 Mesoscale measurements

One main aim of this work has been to try to overcome the scale differences between homogeneous laboratory samples and inverted model cells from field scale tomography.

The scale difference is a challenging problem and in future work, mesoscale SIP measurements could provide an additional important link between laboratory- and field scale SIP measurements. Mesoscale measurements can consist of e.g. borehole SIP logging or small-scale SIP tomography surveys in controlled artificial environments.

8. REFERENCES

Abdel Aal, G. Z., Slater, L. D. and Atekwana, E. A. (2006). Induced-polarization measurements on unconsolidated sediments from a site of active hydrocarbon biodegradation, *Geophysics*, **71**(2), pp. H13–H24.

Archie, G. E. (1942). The Electrical Resistivity Log as an Aid in Determining Some Reservoir Characteristics, *Transactions of the AIME*, **146**, pp. 54–62.

Atekwana, E. A. and Slater, L. D. (2009). Biogeophysics: A new frontier in Earth science research, *Reviews of Geophysics*, **47**(4), pp. 1–30.

Auken, E., Christiansen, A. V., Kirkegaard, C., Fiandaca, G., Schamper, C., Behroozmand, A. A., Binley, A., Nielsen, E., Effersø, F., Christensen, N. B., Sørensen, K., Foged, N. and Vignoli, G. (2014). An overview of a highly versatile forward and stable inverse algorithm for airborne, ground-based and borehole electromagnetic and electric data, *Exploration Geophysics*, **46**(3), pp. 223–235.

Auken, E., Viezzoli, A. and Christiansen, A. V. (2009). A single software for processing, inverting, and presentation of AEM data of different system: The Aarhus Workbench, in *ASEG Expanded Abstracts 2009*, pp. 1–5.

Bard, A. J. and Faulkner, L. R. (2001). *Electrochemical Methods Fundamentals and Applications*. Second edi. John Wiley & Sons, Inc.

Beek, L. Van (1960). The Maxwell-Wagner-Sillars effect, describing apparent dielectric loss in inhomogeneous media, *Physica*, **26**(1), pp. 66–68.

Binley, A., Slater, L. D., Fukes, M. and Cassiani, G. (2005). Relationship between spectral induced polarization and hydraulic properties of saturated and unsaturated sandstone, *Water Resources Research*, **41**(12), p. W12417.

Brotzen, F. (1959). *On Tylocidaris species (Echinoidea) and the stratigraphy of the Danian of Sweden with a bibliography of the Danian and the Paleocene: with a bibliography of the Danian and the Paleocene.* Stockholm: Sveriges Geologiska Undersökning.

Bücker, M., Orozco, A. F., Hördt, A. and Kemna, A. (2017). An analytical membrane-polarization model to predict the complex conductivity signature of immiscible liquid hydrocarbon contaminants, *Near Surface Geophysics*, **15**(6), pp. 547–562.

Bücker, M. and Hördt, A. (2013a). Analytical modelling of membrane polarization with explicit parametrization of pore radii and the electrical double layer, *Geophysical Journal International*, **194**(2), pp. 804–813.

Bücker, M. and Hördt, A. (2013b). Long and short narrow pore models for membrane polarization, *Geophysics*, **78**(6), pp. E299–E314.

Christensen, W. K. (1984). The Albian to Maastrichtian of Southern Sweden and Bornholm, Denmark: a Review, *Cretatceous Research*, **5**, pp. 313–327.

Cole, K. S. and Cole, R. H. (1941). Dispersion and Absorption in Dielectrics I. Alternating Current Characteristics, *The Journal of Chemical Physics*, **9**, pp. 341–351.

Dahlin, T. (2014). Factors affecting time domain IP data quality, in *3rd International Workshop on Induced Polarization, 6 – 9 April 2014 (Ile d'Oléron, France)*, pp. 50–51.

Dahlin, T. and Leroux, V. (2012). Improvement in time-domain induced polarization data quality with multi-electrode systems by separating current and potential cables, *Near Surface Geophysics*, **10**, pp. 545–565.

Dunham, R. J. (1962). Classification of carbonate rocks according to texture, *Classification of carbonate rocks*, **1**, pp. 108–121.

Fiandaca, G., Ramm, J., Binley, A., Gazoty, A., Christiansen, a. V. and Auken, E. (2013). Resolving spectral information from time domain induced polarization data through 2-D inversion, *Geophysical Journal International*, **192**(2), pp. 631–646.

Fiandaca, G. (2018). Induction-free acquisition range in spectral time- and frequency-domain induced polarization at field scale, *Geophysical Journal International*, p. ggy409.

Fiandaca, G., Christiansen, A. V. and Auken, E. (2015). Depth of Investigation for Multi-parameters Inversions, in *Near Surface Geoscience 2015 - 21st European Meeting of Environmental and Engineering Geophysics*, pp. 6–10.

Fiandaca, G., Madsen, L. M. and Maurya, P. K. (2018). Re-parameterizations of the Cole-Cole model for improved spectral inversio of induced polarization data, *Near Surface Geophysics*, **16**, p. in press.

Flügel, E. (2010). *Microfacies of carbonate rocks: Analysis, interpretation and application*. Berlin: Springer Verlag.

Iwamoto, M. (2012). Maxwell–Wagner Effect, in Bhushan, B. (ed.) *Encyclopedia of Nanotechnology*, pp. 1276–1285.

Johansson, S., Fiandaca, G. & Dahlin, T. (2015). Influence of Non-Aqueous Phase Liquid Configuration on Induced Polarization Parameters: Conceptual Models Applied to a Time-Domain Field Case Study. *Journal of Applied Geophysics*, **123**, pp. 295–309.

Johansson, S., Hedblom, P. & Dahlin, T. (2020). Spectral analysis of time domain induced polarization waveforms. Journal of Applied Geophysics, 177. https://doi.org/10.1016/j.jappgeo.2020.10.104037

Johansson, S., Sparrenbom, C., Fiandaca, G., Lindskog, A., Olsson, P.-I., Dahlin, T. & Rosqvist, H. (2016). Investigations of a Cretaceous Limestone with Spectral Induced Polarization and Scanning Electron Microscopy. *Geophysical Journal International*, **208**(2), pp. 954-972.

Johansson, S., Rossi, M., Hall, S. A., Sparrenbom, C., Hagerberg, D., Tudisco, E., Rosqvist, H. & Dahlin, T. (2019a). Combining Spectral Induced Polarization with x-ray tomography to investigate the importance of DNAPL geometry in sand samples. *Geophysics*, **84**(3), pp. E173-E188.

Johansson, S., Lindskog, A., Fiandaca, G. & Dahlin, T. (2019b). Spectral Induced Polarization of limestone: time domain field data, frequency domain laboratory data and physicochemical rock properties. *Geophysical Journal International*, published online, https://doi.org/10.1093/gji/ggz504

Johnson, I. M. (1984). Spectral induced polarization parameters as determined through time-domain measurements, *Geophysics*, **49**(11), pp. 1993–2003.

Kemna, A. (2000). *Tomographic Inversion of Complex Resistivity - Theory and Application*. Ruhr-Universität Bochum.

Kemna, A., Binley, A., Cassiani, G., Niederleithinger, E., Revil, A., Slater, L., Williams, K. H., Orozco, A. F., Haegel, F., Hördt, A., Kruschwitz, S., Leroux, V., Titov, K. and Zimmermann, E. (2012). An overview of the spectral induced polarization method for near-surface applications, *Near Surface Geophysics*, **10**, pp. 453–468.

Koch, K., Kemna, A., Irving, J. and Holliger, K. (2011). Impact of changes in grain size and pore space on the hydraulic conductivity and spectral induced polarization response of sand, *Hydrology and Earth System Sciences*, **15**(6), pp. 1785–1794.

Kornfält, K.-A., Bergström, J., Carserud, L., Henkel, H. and Sundquist, B. (1978). Description to the map of solid rocks and the aeromagnetic map Kristianstad SO, in *Swedish Geological Survey*.

Kruschwitz, S., Binley, A., Lesmes, D. and Elshenawy, A. (2010). Textural controls on low-frequency electrical spectra of porous media, *Geophysics*, **75**(4), pp. WA113-WA123.

Leroy, P., Revil, a, Kemna, a, Cosenza, P. and Ghorbani, a (2008). Complex conductivity of water-saturated packs of glass beads., *Journal of colloid and interface science*, **321**(1), pp. 103–17.

Leroy, P., Revil, A., Kemna, A., Cosenza, P. and Ghorbani, A. (2008). Complex conductivity of water-saturated packs of glass beads, *Journal of Colloid and Interface Science*, **321**(1), pp. 103–117.

Lesmes, D. P. and Morgan, F. D. (2001). Dielectric spectroscopy of sedimentary rocks, *Journal of Geophysical Research*, **106**(B7), pp. 13329–13346.

Lewis, R. G. J. (1985). The determination of spectral parameters with pulse-train induced polarization, *Geophysics*, **50**(5), pp. 870–871.

de Lima, O. A. L. and Sharma, M. M. (1992). A generalized Maxwell-Wagner theory for membrane polarization in shaly sands, *Geophysics*, **57**(3), pp. 431–440.

Madsen, L. M., Fiandaca, G., Auken, E. and Christiansen, A. V. (2017). Time-domain induced polarization - an analysis of Cole-Cole parameter resolution and correlation using Markov ChainMonte Carlo inversion, *Geophysical Journal International*, **211**(3), pp. 1341–1353.

Marshall, D. J. and Madden, T. R. (1959). Induced polarization, a study of its causes, *Geophysics*, **XXIV**(4), pp. 790–816.

Nordsiek, S. and Weller, A. (2008). A new approach to fitting induced-polarization spectra, *Geophysics*, **73**(6), pp. F235–F245.

Olsson, P.-I., Dahlin, T., Fiandaca, G. and Auken, E. (2015). Measuring time-domain spectral induced polarization in the on-time: decreasing acquisition time and increasing signal-to-noise ratio, *Journal of Applied Geophysics*. Elsevier B.V., **123**, pp. 316–321.

Olsson, P.-I., Fiandaca, G., Larsen, J. J., Dahlin, T. and Auken, E. (2016). Doubling the spectrum of time-domain induced polarization: removal of non-linear self-potential drift, harmonic noise and spikes, tapered gating, and uncertainty estimation, *Submitted for publication (Geophysical Journal International)*.

Olsson, P.-I., Fiandaca, G., Larsen, J. J., Dahlin, T. and Auken, E. (2016). Doubling the spectrum of time-domain induced polarization by harmonic de-noising, drift correction, spike removal, tapered gating and data uncertainty estimation, *Geophysical Journal International*, **207**(2), pp. 774–784.

Pelton, W. H., Ward, S. H., Hallof, P. G., Sill, W. R. and Nelson, P. H. (1978). Mineral discrimination and removal of inductive coupling with multifrequency IP, *Geophysics*, **43**(3), pp. 588–609.

Revil, A. and Florsch, N. (2010). Determination of permeability from spectral induced polarization in granular media, *Geophysical Journal International*, **181**(3), pp. 1480–1498.

Schwarz, G. (1962). A theory of the low-frequency dielectric dispersion of colloidal particles in electrolyte solution, *Journal of Physical Chemistry*, **66**(12), pp. 2636–2642.

Scott, J. B. T. and Barker, R. D. (2003). Determining pore-throat size in Permo-Triassic sandstones from low-frequency electrical spectroscopy, *Geophysical Research Letters*, **30**(9), p. 1450.

Seigel, H. O. (1959). Mathematical formulation and type curves for induced polarization, *Geophysics*, **XXIV**(3), pp. 547–565.

Sen, P. N., Scala, C. and Cohen, M. H. (1981). A self-similar model for sedimentary rocks with application to the dielectric constant of fused glass beads, *Geophysics*, **46**(5), pp. 781–795.

Sivhed, U., Wikman, H. and Erlström, M. (1999). *Beskrivning till berggrundskartorna 1C Trelleborg NV and NO samt 2C Malmö SV, SO, NV and NO*.

Slater, L. D. and Glaser, D. R. R. (2003). Controls on induced polarization in sandy unconsolidated sediments and application to aquifer characterization, *Geophysics*, **68**(5), pp. 1547–1558.

Slater, L. D. and Lesmes, D. (2002). IP interpretation in environmental investigations, *Geophysics*, **67**(1), pp. 77–88.

Slater, L. and Lesmes, D. P. (2002). Electrical-hydraulic relationships observed for unconsolidated sediments, *Water Resources Research*. American Geophysical Union, **38**(10), p. 1213.

Slater, L., Ntarlagiannis, D. and Wishart, D. (2006). On the relationship between induced polarization and surface area in metal-sand and clay-sand mixtures, *Geophysics*, **71**(2), pp. A1–A5.

Soininen, H. (1984). Inapplicability of pulse train time-domain measurements to spectral induced polarization, *Geophysics*, **49**(6), p. 826.

Sumner, J. S. (1976). *Principles of induced polarization for geophysical exploration*. Amsterdam: Elsevier Scientific Publishing Company.

Tarasov, A. and Titov, K. (2013). On the use of the Cole-Cole equations in spectral induced polarization, *Geophysical Journal International*, **195**(1), pp. 352–356.

Titov, K., Komarov, V., Tarasov, V. and Levitski, A. (2002). Theoretical and experimental study of time domain-induced polarization in water-saturated sands, *Journal of Applied Geophysics*, **50**(4), pp. 417–433.

Titov, K., Kemna, A., Tarasov, A. and Vereecken, H. (2004). Induced Polarization of Unsaturated Sands Determined through Time Domain Measurements, *Vadose Zone Journal*, **3**(4), pp. 1160–1168.

Tombs, J. M. C. (1981). The feasibility of making spectral IP measurements in the time domain, *Geoexploration*, **19**, pp. 91–102.

Ulrich, C. and Slater, L. (2004). Induced polarization measurements on unsaturated, unconsolidated sands, *Geophysics*, **69**(3), pp. 762–771.

Vanhala, H. (1992). Spectral IP studies of Finnish ore prospects, *Geophysics*, **57**(12), pp. 1545–1555.

Vinegar, H. J. and Waxman, M. H. (1984). Induced polarization of shaly sands, *Geophysics*, **49**(8), pp. 1267–1287.

Van Voorhis, G. D., Nelson, P. H. and Drake, T. L. (1973). Complex resistivity spectra of porphyry copper mineralization, *Geophysics*, **38**(1), pp. 49–60.

Ward, S. (1988). The resistivity and induced polarization methods, in *1st EEGS Symposium on the Application of Geophysics*.

Weller, A., Slater, L., Nordsiek, S. and Ntarlagiannis, D. (2010). On the estimation of specific surface per unit pore volume from induced polarization: A robust empirical relation fits multiple data sets, *Geophysics*, **75**(4), pp. WA105-WA112.

Weller, A., Slater, L., Huisman, J. A., Esser, O. and Haegel, F. (2015). On the specific polarizability of sands and sand-clay mixtures, *Geophysics*, **80**(3), pp. A57–A61.

Weller, A. and Slater, L. (2012). Salinity dependence of complex conductivity of unconsolidated and consolidated materials: Comparisons with electrical double layer models, *Geophysics*, **77**(5), pp. D185–D198.

Weller, A. and Slater, L. D. (2015). Induced polarization dependence on pore space geometry : Empirical observations and mechanistic predictions, *Journal of Applied Geophysics*. Elsevier B.V., **123**, pp. 310–315.

Wong, J. (1979). An electrochemical model of the induced-polarization phenomenon in disseminated sulfide ores, *Geophysics*, **44**(7), pp. 1245–1265.

Zimmermann, E., Kemna, a, Berwix, J., Glaas, W., Münch, H. M. and Huisman, J. a (2008). A high-accuracy impedance spectrometer for measuring sediments with low polarizability, *Measurement Science and Technology*, **19**(10), p. 105603.

Zisser, N., Kemna, A. and Nover, G. (2010). Relationship between low-frequency electrical properties and hydraulic permeability of low-permeability sandstones, *Geophysics*, **75**(3), pp. E131–E141.

BeFo

Box 5501
SE-114 85 Stockholm

info@befoonline.org • www.befoonline.org
Visiting address: Storgatan 19, Stockholm

ISSN 1104-1773